Photometric observations of the binary near-Earth asteroid (65803) Didymos in 2015-2021 prior to DART impact

P. Pravec [a], C. A. Thomas [b], A. S. Rivkin [c], P. Scheirich [a], N. Moskovitz [d], M. M. Knight [e,f], C. Snodgrass [g], J. de León [h], J. Licandro [h], M. Popescu [i,h], A. Thirouin [d], D. Föhring [j,k], C. O. Chandler [b], W. J. Oldroyd [b], C. A. Trujillo [b], E. S. Howell [ℓ], S. F. Green [m], J. Thomas-Osip [n], S. S. Sheppard [o], T. L. Farnham [f], E. Mazzotta Epifani [p], E. Dotto [p], S. Ieva [p], M. Dall'Ora [q], R. Kokotanekova [r,s], B. Carry [t], D. Souami [u,v]

[a] *Astronomical Institute, Academy of Sciences of the Czech Republic, Fričova 1, CZ-25165 Ondřejov, Czech Republic*

[b] *Department of Physics and Astronomy, Northern Arizona University, PO Box 6010, Flagstaff, AZ 86011, USA*

[c] *JHU/APL, 11100 Johns Hopkins Rd, Laurel, MD 20723, USA*

[d] *Lowell Observatory, 1400 W Mars Hill Road, Flagstaff, AZ 86001, USA*

[e] *Department of Physics, United States Naval Academy, 572C Holloway Road, Annapolis, MD 21402, USA*

[f] *University of Maryland, Department of Astronomy, College Park, MD 20742, USA*

[g] *Institute for Astronomy, University of Edinburgh, Royal Observatory, Edinburgh EH9 3HJ, UK*

[h] *Instituto de Astrofísica de Canarias (IAC), C/Vía Láctea s/n, 38205 La Laguna, Spain*

[i] *Astronomical Institute of the Romanian Academy, 5 Cuţitul de Argint, 040557 Bucharest, Romania*

[j] *Institute for Astronomy, University of Hawai'i, 2680 Woodlawn Drive, Honolulu, HI 96822, USA*

[k] *ESA NEO Coordination Centre, Largo Galileo Galilei, 1, 00044 Frascati (RM), Italy*

[ℓ] *Lunar and Planetary Laboratory, University of Arizona, Tucson, AZ 85721, USA*

[m] *School of Physical Sciences, The Open University, Milton Keynes, MK7 6AA, UK*

[n] *Gemini Observatory/NSF's NOIRLab, Casilla 603, La Serena, Chile*

[o] *Carnegie Institution for Science, Earth and Planets Laboratory, 5241 Broad Branch Rd. NW, Washington, DC 20015, USA*

[p] *INAF – Osservatorio Astronomico di Roma, Via Frascati 33, 00040 Monte Porzio Catone (RM), Italy*

[q] *INAF – Osservatorio Astronomico di Capodimonte, Salita Moiariello 16, 80131 Napoli, Italy*

[r] *European Southern Observatory, Karl-Schwarzschild-Str 2, 85748 Garching, Germany*

[s] *Institute of Astronomy, Bulgarian Academy of Sciences, Sofia, Bulgaria*

[t] *Université Côte d'Azur, Observatoire de la Côte d'Azur, CNRS, Laboratoire Lagrange, France*

[u] *LESIA, Observatoire de Paris, Université PSL, Sorbonne Université, Université de Paris, CNRS, 92190 Meudon, France*

[v] *naXys, University of Namur, 8 Rempart de la Vierge, Namur, B-5000, Belgium*

Revised, 2022 June

Editorial correspondence to:
Dr. Petr Pravec
Astronomical Institute AS CR
Fričova 1
Ondřejov
CZ-25165
Czech Republic
Phone: 00420-323-620352
Fax: 00420-323-620263
E-mail address: petr.pravec@asu.cas.cz

Abstract

We performed photometric observations of the binary near-Earth asteroid (65803) Didymos in support of the Double Asteroid Redirection Test (DART) mission that will test the Kinetic Impactor technology for diverting dangerous asteroids. It will hit the Didymos secondary, called Dimorphos, on 2022-09-26. We observed Didymos with 11 telescopes with diameters from 3.5 to 10.4 m during four apparitions in 2015–2021, obtained data with root-mean-square residuals from 0.006 to 0.030 mag. We analyzed the lightcurve data and decomposed them into the primary rotational and the secondary orbital lightcurves. We detected 37 mutual eclipse/occultation events between the binary system components. The data presented here, in combination with 18 mutual events detected in 2003 (Pravec et al., Icarus 181, 63-93, 2006) provide the basis for modeling the Dimorphos orbit around the Didymos primary. The orbit modeling is discussed in detail by Scheirich&Pravec (PSJ, **in press**) and Naidu et al. (PSJ, submitted). The primary lightcurves were complex, showing multiple extrema, on some epochs. They suggest a presence of complex topography on the primary's surface that is apparent in specific viewing/illumination geometries; the primary shape model by Naidu et al. (Icarus 348, 113777, 2020) needs to be refined. The secondary rotational lightcurve data were limited and did not provide a clear solution for the rotation period and equatorial elongation of Dimorphos. We define requirements for observations of the secondary lightcurve to provide the needed information on Dimorphos' rotation and elongation when Didymos is bright in July-September 2022 before the DART impact.

Key words: Asteroids, satellites; Photometry; DART space mission; Hera space mission

1 Introduction

The near-Earth asteroid (65803) Didymos, originally designated 1996 GT, was discovered by the *Spacewatch* asteroid survey from Kitt Peak Observatory in Arizona on 1996 April 11. Seven years later it was thoroughly studied with photometric and radar observations around and after its close approach to Earth in November 2003, which led to the discovery of its satellite with photometric observations taken from Ondřejov Observatory, Carbuncle Hill Observatory and Steward Observatory during 2003 November 20–24 and with radar observations from Arecibo on 2003 November 23 and 24 (Pravec et al., 2003). The photometric observations were analyzed and modeled in Pravec et al. (2006) and Scheirich and Pravec (2009), where they published initial estimates of several parameters of the binary asteroid system, including first estimates of the secondary (satellite) orbit around the primary body of the binary system. The radar observations were published and modeled together with the photometric data by Naidu et al. (2020) who obtained a shape model of the primary and determined or constrained several parameters of the binary asteroid system. The current best estimates for parameters of the primary, the secondary, and their mutual orbit are given in Scheirich and Pravec (2022), and we give the nominal values for some of them in following. The volume-equivalent diameters of the primary and the secondary are 0.78 and 0.17 km, respectively. The geometric albedo in the V band is 0.15. The mutual orbit is retrograde with the J2000 ecliptic coordinates of the pole $(L_{\rm P}, B_{\rm P}) = (320.6°, -78.6°)$, with a semimajor axis of 1.19 km and an orbital period of 11.9216 h. Spectral observations taken in 2003 originally classified Didymos as an Xk type (Binzel et al., 2004), but later analyses led to a consensus on a silicate composition for the binary system (de León et al., 2006, 2010; Dunn et al., 2013). New spectral observations obtained in 2021 have confirmed its silicate nature, with hints of possible small spectral variability with the primary's rotation (Ieva et al., 2022).

The secondary of the Didymos binary system, recently named Dimorphos, has been selected as a target of the Double Asteroid Redirection Test (DART). DART is NASA's first planetary defense test mission, demonstrating the kinetic impactor mitigation technique. It launched from Vandenberg Space Force Base in November 2021 and will arrive at the Didymos system and impact into Dimorphos on 2022 September 26. The main benefit of using a binary asteroid system for a kinetic impactor mission is that it allows the results of the test to be measured from Earth via photometric measurements, assuming that the binary system exhibits mutual events seen from Earth. [1] Mutual events in the Didymos system can be seen from Earth, making it a suitable target. Rivkin et al. (2021) discuss the factors that led to the recognition that Didymos was the best candidate for a kinetic impactor test, and its selection as the DART target system. Several years after the DART impact the Didymos system will

[1] DART will also perform a limited characterization of the Didymos system around the impact time. It will carry the ASI Light Italian Cubesat for Imaging of Asteroid (LICIACube) (Dotto et al., 2021) as a piggyback. The LICIACube will perform an autonomous flyby of the Didymos system probing the DART impact and it will study the structure and evolution of the ejecta plume produced by the impact, which is expected to bring fundamental information for the determination of the momentum transfer induced by DART.

be visited by ESA's Hera mission that will provide a thorough description of the post-impact state of the binary system (Michel et al., 2022).

An important part of the preparation of the DART mission has been an observational effort to determine parameters of the binary asteroid system. The most significant mission-critical task has been the effort to precisely determine the orbit of the secondary around the primary. For that, we have used the method of photometric observations of mutual events between binary asteroid system components (Pravec et al., 2006), which we have applied to photometric observations taken with several large– or medium–sized ground–based telescopes from 2015 to 2021. In this paper, we present results of this major observational campaign. The photometric observations are presented in Section 2. In Section 3, we present decompositions of the photometric data into the primary rotational and secondary orbital lightcurve components for individual epochs covered by the observations. The data for mutual events between the two bodies of the binary asteroid obtained from the derived secondary orbital lightcurve components have been used for modeling the secondary orbit by Scheirich and Pravec (2022) and Naidu et al. (2022). In Section 4, we analyze constraints provided by the secondary rotational lightcurve data (outside mutual events) on equatorial elongation of the secondary.

2 Observations

The photometric observations taken in the Dimorphos discovery apparition in 2003 were published in Pravec et al. (2006). We summarize them in the first part of Table 1. The observations were taken with small telescopes with diameters from 0.35 to 1.5 m and, thanks to the high brightness of Didymos in the favorable observing conditions shortly after its close approach to Earth in November 2003, with visual magnitude V in the range from 12.9 to 14.9, they were of high quality; the median rms residual of Fourier series fits to them is 0.008 mag (see Section 3). As will be seen below, the 2003 data are the highest–quality data subset of all the five observed apparitions of Didymos and the second most abundant (after the last apparition of 2020–2021) in number of observed mutual events. In addition, these data were taken with Didymos at heliocentric true anomaly values from 27° to 53° which were not covered in the 2015-2021 apparitions. Thus, the 2003 data provided a great baseline for accurate determination of Dimorphos' orbit.

Shortly after the satellite of the Didymos binary system was selected as the target of the DART mission, we realized the need to make many more photometric observations in order to determine its mutual orbit with high accuracy. As Didymos' heliocentric orbit period is 2.109 yr, its oppositions with the Sun occurred at nearly 2-year intervals during 2015–2021. (The heliocentric synodic period of Didymos is $(1-2.109^{-1})^{-1} = 1.902$ yr.) Unlike in the 2003 apparition when Didymos was near perihelion and close to Earth and thus very bright, it was much more distant during the years 2015–2021; the four oppositions in 2015, 2017, 2019 and 2021 occurred at heliocentric true anomalies $> 119°$, i.e., Didymos was far from the perihelion of its eccentric orbit ($e = 0.384$). It was therefore much fainter during the four follow-up apparitions than in 2003, with V in the range from 19.0 to 21.5 on individual observing nights.

We therefore required medium– to large–size telescopes to obtain data of acceptable quality for the task of detecting mutual events in the binary system and modeling Dimorphos' orbit around the primary.

The observations are summarized in Table 1. Each row in the table represents one nightly run with one telescope, identified with the mid-UTC date of the session rounded to the nearest tenth of a day in the first column. Subsequent columns give the telescope or station name, the telescope's diameter, the number of photometric data points obtained, the duration of the session, and a reference to where more information on the observations is available.

As shown in Table 1, the first photometric observations since 2003 were taken with the 4.3-m Discovery Channel Telescope (which has since been renamed as the Lowell Discovery Telescope) in Arizona on two nights in April 2015. They gave only a limited quantity of medium-quality data with an rms residual of 0.024 mag (see the analysis in Section 3 and Table 2) and we realized that we would need to take many more data and use larger telescopes, or medium–size telescopes in excellent observing conditions, to obtain the required high-quality data for Didymos in following apparitions. In 2017 we used several telescopes with sizes from 3.5 to 10.4 m and obtained more abundant data, although their quality was largely similar to that of the 2015 observations. We succeeded in obtaining high-quality observations with a median rms residual of 0.010 mag in 2019, although the limited coverage only allowed the detection of 5 events (see Table 2). Learning from the experience of the 2015 to 2019 apparitions, in 2020–2021 we obtained much wider data coverage (detecting as many as 23 events) with high quality (the median rms residual was 0.011 mag).

In the following subsections, we describe the observational and reduction techniques we used on the 11 telescopes involved in the observational campaign. We used some common techniques for all or most of the observations, but there were many differences in the observing strategies and reduction techniques used on the individual telescopes or by the individual observers, and we used several different photometric reduction methods and tools. By that, we effectively checked mutual consistency of the obtained data, eliminating or reducing the possibility of presence of systematics in the data that could come from using a single observational technique and reduction pipeline. The common points for all the observations were: We used CCD detectors, processed the obtained images with standard bias subtraction and flatfield correction routines, and performed aperture photometry on Didymos and reference star images. In the subsections below, we focus primarily on the specifics of the individual observations and data reductions.

Table 1: Photometric observations of (65803) Didymos

Session mid-UT	Station/Telescope	Diam. (m)	Points	Dur. (hr)	Ref.
2003-11-20.9	Ondřejov	0.65	296	4.1	P06
2003-11-22.0	Ondřejov	0.65	315	6.0	P06
2003-11-22.2	Carbuncle Hill	0.35	102	5.6	P06
2003-11-23.2	Carbuncle Hill	0.35	89	4.8	P06
2003-11-24.2	Mt. Lemmon	1.5	252	6.2	P06
2003-11-24.3	Carbuncle Hill	0.35	57	3.4	P06
2003-11-26.2	Carbuncle Hill	0.35	97	5.8	P06
2003-11-27.9	Ondřejov	0.65	146	4.2	P06
2003-11-30.0	Ondřejov	0.65	283	8.2	P06
2003-12-02.2	Carbuncle Hill	0.35	79	5.0	P06
2003-12-03.3	Palmer Divide	0.50	106	7.8	P06
2003-12-04.1	Carbuncle Hill	0.35	67	5.6	P06
2003-12-16.9	Ondřejov	0.65	15	0.8	P06
2003-12-17.3	Palmer Divide	0.50	146	9.2	P06
2003-12-18.9	Ondřejov	0.65	95	10.0	P06
2003-12-19.3	Palmer Divide	0.50	75	7.7	P06
2003-12-20.3	Palmer Divide	0.50	127	7.1	P06
2015-04-13.3	DCT	4.3	75	5.7	Sect. 2.1
2015-04-14.4	DCT	4.3	45	1.7	Sect. 2.1
2017-02-23.3	VLT	8.2	17	0.7	Sect. 2.2
2017-02-24.4	VLT	8.2	15	0.6	Sect. 2.2
2017-02-25.1	GTC	10.4	75	5.5	Sect. 2.3
2017-02-25.4	VLT	8.2	17	0.7	Sect. 2.2
2017-02-25.5	MMT	6.5	137	4.2	Sect. 2.4
2017-02-27.3	VLT	8.2	31	1.5	Sect. 2.2
2017-03-01.3	VLT	8.2	12	0.6	Sect. 2.2
2017-03-31.1	WHT	4.2	100	8.9	Sect. 2.5
2017-04-01.3	VLT	8.2	27	1.6	Sect. 2.2
2017-04-02.3	VLT	8.2	17	0.7	Sect. 2.2
2017-04-18.2	DCT	4.3	66	5.2	Sect. 2.1
2017-04-27.1	NTT	3.5	108	6.9	Sect. 2.6
2017-05-04.3	Gemini N	8.1	59	3.8	Sect. 2.7

Session mid-UT	Station/Telescope	Diam. (m)	Points	Dur. (hr)	Ref.
2019-01-31.4	DCT	4.3	98	5.6	Sect. 2.1
2019-02-02.2	Magellan	6.5	21	1.3	Sect. 2.8
2019-03-09.1	GTC	10.4	166	6.5	Sect. 2.3
2019-03-10.2	GTC	10.4	65	3.2	Sect. 2.3
2019-03-11.1	GTC	10.4	143	6.6	Sect. 2.3
2020-12-12.6	Gemini N	8.1	89	4.1	Sect. 2.7
2020-12-17.4	LDT	4.3	95	5.3	Sect. 2.1
2020-12-20.5	LDT	4.3	31	2.2	Sect. 2.1
2020-12-23.4	LDT	4.3	118	5.8	Sect. 2.1
2021-01-08.5	LDT	4.3	93	4.8	Sect. 2.1
2021-01-09.4	LDT	4.3	118	6.0	Sect. 2.1
2021-01-10.4	LDT	4.3	78	4.8	Sect. 2.1
2021-01-12.6	Gemini N	8.1	107	4.5	Sect. 2.7
2021-01-14.4	LDT	4.3	107	5.9	Sect. 2.1
2021-01-14.6	Keck	10.0	69	4.4	Sect. 2.9
2021-01-17.5	Gemini N	8.1	142	5.5	Sect. 2.7
2021-01-18.4	LBT	8.4	150	3.0	Sect. 2.10
2021-01-20.2	TNG	3.6	296	6.5	Sect. 2.11
2021-02-17.4	LDT	4.3	121	9.4	Sect. 2.1
2021-03-06.3	LDT	4.3	149	8.2	Sect. 2.1

Note: P06 is Pravec et al. (2006).

2.1 Lowell Discovery Telescope (Discovery Channel Telescope)

The 4.3-m Lowell Discovery Telescope (LDT, known prior to February 2020 as the Discovery Channel Telescope, DCT) is located near Happy Jack, Arizona at an elevation of 2360 m. Images of Didymos were obtained from LDT in every apparition from 2015 to 2021 (Table 1). In all cases, the Large Monolithic Imager (LMI), which is equipped with a $6\mathrm{k} \times 6\mathrm{k}$ e2v CCD, was used with a broadband *VR* filter (covering the wavelengths between about 500 and 700 nm) to maximize signal-to-noise ratio. LMI images a 12.3-arcmin square field-of-view that is sampled at an image scale of 0.12 arcsec/pixel. All images were obtained in 3×3 binning mode resulting in an effective image scale of 0.36 arcsec/pixel. For all nights except for 2021-03-06, the telescope was tracked at sidereal rates, allowing the asteroid to move through a fixed star field. On 2021-03-06 the telescope was tracked at one half the non-sidereal rates so that both stars and asteroid were trailed by the same amount (roughly 1 arcsec). Exposure times ranged from 120 to 180 seconds, chosen to minimize trailing based on the non-sidereal motion of the asteroid and local seeing conditions. Across all

apparitions, any images affected by background contamination and/or heavy extinction were removed from further analysis.

The data from 2015-04-14 and 2017-04-18 were analyzed using the standard data reduction described in Thirouin and Sheppard (2018). To summarize our approach; we selected an optimal aperture using the growth curve technique (Stetson, 1990) to limit background contamination while including all of the object's flux. Aperture photometry with the optimal aperture radius was performed with the DAOPHOT routines (Stetson, 1987). The data from 2015-04-13 were reduced at Ondřejov Observatory using an analogous optimal aperture-photometry method using their *Aphot* software package (Pravec et al., 2006).

The measurement of photometry from the 2019 and 2020–2021 apparitions involved processing images with the PhotometryPipeline (Mommert, 2017). This pipeline registers images using Scamp (Bertin, 2006) with the Gaia DR2 reference catalog (Gaia Collaboration, 2018). Point source photometry is measured using SourceExtractor (Bertin and Arnouts, 1996). Calibration of the photometry involved converting instrumental to calibrated magnitudes based on field stars with solar-like colors (within 0.2 magnitudes of the Sun's SDSS $(g-r)$ and $(r-i)$ color indices) in the PanSTARRS DR1 catalog (Flewelling et al., 2020). The photometry was calibrated to the PanSTARRS r-band. In general, about 10 field stars were used to calibrate each frame. An optimized aperture was chosen for each night of observing that minimized errors associated with the zero point calibration (i.e., tying to the reference catalog) and the measured instrumental magnitudes. These apertures ranged from 3.26 to 6.63 pixels (1.17 to 2.39 arcsec) in radius. Though not critical for the differential analysis performed here (Section 3), this resulted in absolute photometric calibration with errors about 0.02 mag.

In total the LDT data provided lightcurves from 13 different nights and sampled part of or the entirety of 16 individual mutual events. Lightcurve quality from LDT was good on most nights, with the median rms residual relative to best fits of the primary lightcurve of 0.011 mag (see Section 3). The apparent V magnitude of Didymos during these LDT observations ranged from a minimum of about 19.0 in February 2021 to a maximum of about 21.0 in April 2017.

2.2 Very Large Telescope

Observations in 2017 were taken at Unit Telescope 3 (Melipal; UT3) of the European Southern Observatory (ESO) 8-m Very Large Telescope (VLT) using the VIMOS instrument (Le Fèvre et al., 2003). This instrument is primarily a multi-object spectrograph, but also has an imaging mode with an array of four CCDs, each with a 7×8 arcmin^2 field of view and 0.21 arcsec/pixel scale, and standard *UBVRI* filters. Didymos was observed in service mode in a programme designed to take advantage of time with relatively poor conditions (for Paranal), when the other instruments on UT3, requiring exceptional seeing, could not be used. Observations were scheduled as independent hour-long blocks, each made up of 17×120 s R-band exposures, tracking the asteroid at its non-sidereal rate. The telescope was offset to have the asteroid appear

approximately in the centre of one of the four CCDs. 13 blocks were taken between 2017-01-14 and 2017-04-03. The seeing (measured by the Paranal site DIMM) varied between 0.36 arcsec and 3.2 arcsec, with a median of 1.2 arcsec, during the exposures. Useful data were obtained on 7 separate nights, on two of which two observing blocks were executed sequentially to have around 1.5 h of continuous exposures (see Table 1). Aperture photometry was performed using IRAF, using apertures with a radius of 1.5 times the frame FWHM, and calibrated using field stars from the Pan-STARRS PS1 catalogue (hereafter PS1; Chambers et al., 2016), after first converting catalogue magnitudes to *UBVRI*. Frames where the asteroid was close to any background source were manually removed from the final lightcurve.

2019 VLT data were taken with FORS on UT1 (Antu), which has a square field of view 6.8 arcmin on each side, across two CCDs, and a (2×2 binned) pixel scale of 0.25 arcsec/pixel (Appenzeller et al., 1998). These observations were performed in visitor mode over the nights of 2019-04-05 and 06, with excellent conditions. A total of 511 exposures were taken over the two nights, the majority with a 50 s exposure time, in the FORS *R_SPECIAL* filter, which is close to the standard Bessell R in wavelength range, but with higher peak transmission and sharper cut-offs, particularly at the red end. Basic data reduction was performed using PyRAF tasks, and photometry was calibrated via field stars appearing in the PS1 catalogue, following the techniques described by Kokotanekova et al. (2017). Unfortunately, the presence of reflections from a nearby bright star influenced the photometry and prevented us from achieving the necessary accuracy to separate the primary lightcurve and mutual events, so this data set is not included in the rest of the analysis.

2.3 Gran Telescopio Canarias

Observations with the Gran Telescopio Canarias (GTC) were done in February 2017 and in March 2019 when the asteroid had apparent visual magnitude $V = 21.0$ and 19.9, respectively. GTC is located at the Roque de Los Muchachos Observatory in La Palma, Canary Islands (Spain), and managed by the Instituto de Astrofísica de Canarias. Images of Didymos were acquired using the Optical System for Imaging and Low Resolution Integrated Spectroscopy (OSIRIS) camera spectrograph (Cepa et al., 2000; Cepa, 2010). It consists of a mosaic of two Marconi CCD detectors, each with 2048×4096 pixels and a total field of view of 7.8×7.8 arcmin^2, providing a plate scale of 0.127 arcsec/pix. To increase the signal-to-noise ratio (S/N) we used 2×2 binning and the standard operation mode with a readout speed of 200 kHz (gain 0.95 e$^-$/ADU, readout noise 4.5 e$^-$).

In 2017 we observed Didymos on 2017-02-25 from 00:26 to 06:00 UT. A series of images of 180 s exposure time were obtained using the Sloan r' filter with the telescope tracking on the asteroid. The observations were run during dark time, with clear skies and at elevations $> 30°$ and a seeing that varied from 0.9 to 1.4 arcsec. In the 2019 apparition observations were carried out on three consecutive nights 2019-03-09, 10 and 11. Observational strategy consisted of identifying the asteroid in the field and placing it in one of the extremes of the CCD, so images were acquired sequentially and with sidereal tracking while the asteroid was crossing the detector. (Didymos had a differential rate of

about 1 arcmin/h and thus the same field was imaged for the entire nightly run.) Sloan r' filter was used and exposure time was fixed to 90 s. The average seeing varied between 1 and 2.5 arcsec, depending on the object airmass and atmosphere variation. The asteroid was observed during dark time and with clear skies. On average, the object was observed when it had a local elevation $> 35°$, i.e., from $\sim$ 22:20 UT to $\sim$ 05:10 UT, with the exception of the second night 2019-03-10 when a high speed wind prevented observations until 02:10 UT.

The data reduction was performed using Image Reduction and Analysis Facility (IRAF v2.16) processing packages (Tody 1986, 1993). APPHOT was used to perform the photometry. The APPHOT is a part of the NOAO.DIGIPHOT package and it includes tools to locate and compute the center of the sources, to fit the sky and to perform aperture photometry. Photometry of the 2017 data was performed with a fixed photometric aperture of radius 2.7 arcsec, with relative calibration between frames calculated using a set of between 9 and 24 field stars (depending on how many of a selected subset of bright and well isolated nearby stars were visible in each frame, as the telescope tracked the asteroid). For the 2019 observations where the field did not change during each nightly run, the following steps were performed for each night's data. First, the asteroid was identified in the first and the last image. These two points were fitted with a straight line and an approximate position of Didymos was calculated with the interpolation on each individual image. Second, PHOT task was applied to each image for retrieving the corresponding magnitude. Three apertures with a 7, 8 and 9 pixel radius were used. The same procedure was applied for 9 reference stars in the field, which were selected to have brightness similar to the asteroid. To compute the differential magnitudes of the asteroid, the reference stars were monitored against their median to remove possible variable ones (this procedure was repeated several times). The final differential magnitude was computed as the difference between the median of the best reference stars and the asteroid magnitude. The reported differential magnitudes represent the median values of the magnitudes computed using all three apertures. All the data points were carefully checked and those affected by background sources were removed (they were about 5% of all points). The photometric errors were estimated by considering the dispersion of points acquired within short time intervals (3 to 5 min). The median values of these are 0.008, 0.009 and 0.011 mag for the 2019-03-09, 10 and 11 runs, respectively.

2.4 Multiple Mirror Telescope

We obtained observations using the Multiple Mirror Telescope (MMT) Observatory 6.5m on Mt. Hopkins south of Tucson, AZ on 2017-02-25, 2017-03-06 and 2019-03-02. Only the data from 2017-02-25 was of sufficient quality for use, and is described here. The seeing was excellent on that night, which turned out to be critical. We obtained 144 images of 100 s each using the MMTCAM and an SDSS r filter. The detector is a 2048×2048 pixels back illuminated CCD with a field of view of 2.7×2.7 arcmin. The images were 1024×1024 pixels having been binned on the chip 2×2. The resulting resolution was 0.16 arcsec/pixel. The telescope was tracking the asteroid but very little trailing was apparent for the star images. The field was dithered by about 20 arcseconds

in RA and Dec about every 30 minutes, and rotated by 90° half-way through the night. Sufficient field stars were available and could be linked through the night. The sky flats were determined to not be sufficient, so a median flat was constructed from the images. We used the standard aperture photometry routines in IRAF with an aperture of 6 pixel radius. The sky annulus had **an inner** radius of 12 pixels and was 6 pixels wide, and outliers were removed using a 3-σ clipping algorithm. **The sky value was computed as the centroid of the distribution after bad pixels were removed. (We note that the sky value computation converged quickly and it appeared adequate for these data. The chip is very uniform and only removal of cosmic rays from the sky pixel distribution was needed to obtain good relative photometry.)** We determined relative magnitudes with the normalized average of the best two field stars at any given time. The chosen stars were at or slightly brighter than Didymos ($V = 19.3$ to 21.5). The formal uncertainties range from 0.024 to 0.045 mag and we adopt a standard deviation of 0.032 mag for the instrumental magnitudes. This is the unweighted standard deviation of all the measurements.

2.5 William Herschel Telescope

Observations were obtained on the night of 2017-03-31 using the ACAM imager on the 4.2-m William Herschel Telescope (WHT). ACAM is mounted at the Cassegrain focus and has a circular field of view of diameter 8.3 arcmin with pixel scale 0.25 arcsec/pixel. Lightcurves were obtained in the Sloan r filter, with occasional frames taken with the Sloan g filter to ascertain colors of Didymos and comparison stars. The exposure time was 180 seconds for all frames. The telescope tracking was set at half the asteroid rate of motion in an attempt to produce equivalent PSFs for Didymos and comparison stars. Image processing and calibration was performed using AstroImageJ (Collins et al., 2017).

The night was non-photometric with variable cirrus. Variations in transmission were typically in the range 0 to 0.3 mag but occasionally exceeding 1 magnitude for a period of several frames. Seeing varied during the night from ~ 0.8 to ~ 1.3 arcsec. With half tracking rate the stellar and asteroid images gave fairly constant equivalent FWHM of ~ 6 pixels (1.5 arcsec). However, several frames were trailed due to lost autoguider signal, and it became apparent that the actual tracking was not accurate enough to ensure consistent PSFs between stars and asteroid, precluding use of small aperture radii for photometry. Multi-aperture tests indicated an optimal choice of 10 pixel radius (2.5 arcsec).

A test for differential extinction using relative colors of field stars showed no detectable effect, so all unsaturated field stars at least two magnitudes brighter than Didymos that were within the field for at least half the night were used for calibration. None of the 12 suitable stars showed relative variability. For any given frame typically 7 to 9 stars were observed and used to construct a synthetic comparison star. Resultant uncertainties in the synthetic star instrumental magnitudes were generally ~ 0.001 mag and always less than 0.003 mag. Overall uncertainties are dominated by Didymos photon noise and background subtraction.

Images were removed from the sequence for a variety of reasons: close proximity to background stars; trailed images; cosmic ray superimposed on asteroid image; cloud extinction causing uncertainties greater than 0.045 magnitude. Of the 166 r frames obtained, 100 were used in the lightcurve analysis (Section 3).

Using PS1 catalogue magnitudes for the field stars, we determined color terms for the ACAM system, and derived a Didymos colour of $(g-r)_{\rm PS1} = 0.52\pm0.04$ and a mean magnitude of $r_{\rm PS1} = 18.23\pm0.01$. Using transformation coefficients from Tonry et al. (2012) we derive a mean Johnson V magnitude of 18.48 ± 0.02.

2.6 New Technology Telescope

Observations with the 3.6-m ESO New Technology Telescope (NTT) were performed using the EFOSC2 instrument (Buzzoni et al., 1984), which provides a 4.1 arcmin field of view and 0.24 arcsec pixels in 2×2 binned readout (Snodgrass et al., 2008). Two runs were performed in April 2017, both in visitor mode: 79 exposures were taken on the night of 2017-04-02, with 300 s exposure times. Conditions were good, but unfortunately Didymos was near a faint star during the mutual event that night and the data are not used in the rest of the analysis. 162 exposures were taken over three consecutive nights from the 24th of April, with the useful data being the 108 frames acquired on the last night of 2017-04-27, with seeing around 0.7 arcsec FWHM (conditions on the first two nights were poor, and limited data were collected). Images were taken through an SDSS r-band filter, with exposure times of 180 s, and the telescope tracking at half the asteroid's non-sidereal rate. Data reduction and photometry were performed using IRAF tasks; photometry was calibrated against field stars from the PS1 catalogue.

2.7 Gemini North Telescope

Observations of Didymos were obtained with the 8.1-m Gemini North Telescope in Hawai'i using the Gemini Multi-Object Spectrograph (GMOS; Hook et al., 2004) in imaging mode on the nights of 2017-05-04, 2020-12-12, 2021-01-12, and 2021-01-17. In all cases, the Sloan i' filter was used to maximize throughput given the redder than solar color $(V - I) = 0.82$ of Didymos (Kitazato et al. 2004). GMOS has a 5.5 arcmin square field-of-view, and with 2×2 binning, a pixel scale of 0.16 arcsec/pixel.

For the night of 2017-05-04, the telescope was tracked at Didymos rates of motion and exposure times of 200 s were used. The night was photometric and the seeing varied between ~ 0.5 arcsec and ~ 0.7 arcsec. The data was reduced using standard methods with the Gemini IRAF package.[2] Differential aperture photometry was performed with AstroPy 2.0.2 (Astropy Collaboration et al., 2018) and its Affiliated package PhotUtils 0.4 (Bradley et al., 2017). Elliptical apertures were used for the 9 trailed SDSS reference stars. Tests with multiple apertures indicated optimal S/N with an aperture of radius 1.5 FWHM of the PSF. The final lightcurve was an average of the differential photometry calculated with the two closest (and most stable) reference stars. A median

[2] `https://ui.adsabs.harvard.edu/abs/2016ascl.soft08006G`

lightcurve using all 9 reference stars was noisier due to the fact that most of them were also fainter than the two closest reference stars.

On each of the nights 2020-12-12, 2021-01-12 and 2021-01-17 a sequence of observations was executed for a duration of 4.1 h, 4.5 h and 6.1 h, respectively, corresponding to 141, 183 and 240 images in turn. (Observations taken on 2020-12-10 were not usable due to a pointing error.) The final numbers of usable data points were 89, 107 and 142, respectively; a significant fraction of data points has been removed during the reduction process as they were affected by less ideal sky conditions, intereferences with background sources or other observational issues. Exposure times of 70 s were used in December and 50 s in January, as the object brightened from $V = 20.0$ to 19.5. The telescope tracking was set to sidereal, while the telescope was repositioned every hour to keep the target centered on the CCD chip. The sky brightness was 50-percentile, while the weather constraints were 70-percentile cloud cover and 85-percentile image quality. [3]

We carried out four independent methods of data reduction and analysis for the 2020 December and 2021 January observations. We determined the approach which started by making use of Theli3 [4] (Schirmer, 2013) provided the best results. We began by visually inspecting portable network graphics (PNG) format images enhanced following the method described in Chandler et al. (2018). We noted significant guide probe interference on night 2020-12-12 and identified potential photometric contaminants (e.g., cosmic rays, background source blending) in 149 of the 564 images of Didymos. Making use of the Theli3 software package we executed a series of data reduction steps, including overscan correction, bias subtraction, flattening of fields, background correction, and collapse correction. We conducted astrometry and embedded updated World Coordinate System (WCS) with Theli3 and/or AstrometryNet (Lang et al., 2010) or PhotometryPipeline (Mommert, 2017). Both Theli3 and PhotometryPipeline query the Vizier catalog service (Ochsenbein et al., 2000). The catalogs we queried were the Sloan Digital Sky Survey Data Release 9 (SDSS DR-9, Ahn et al., 2012), Gaia Data Release 2 (Gaia Collaboration et al., 2018) and Gaia Early Data Release 3 (Gaia Collaboration et al., 2021). Following Chandler et al. (2018) we extracted thumbnail images of Didymos to check for any additional image artifacts and confirm WCS validity. The final version of photometry we produced made use of PhotometryPipeline. We note that while it would be ideal to limit photometric calibration to field stars with similar colors to those of Didymos ($U - B = 0.211 \pm 0.032, B - V = 0.795 \pm 0.016, V - R = 0.458 \pm 0.009$ and $V - I = 0.820 \pm 0.009$, Kitazato et al., 2004) there were insufficient field stars available. We selected the PS1 photometry (Tonry et al., 2012) because of the availability of calibration stars. We manually checked photometry with Aperture Photometry Tool (Laher et al., 2012) on a case-by-case basis. We also used the catalog tool within DS9 to check reference star photometry.

[3] See http://www.gemini.edu/observing/telescopes-and-sites/sites for explanation of the use of percentiles for the Gemini weather conditions.

[4] `https://github.com/schirmermischa/THELI`

2.8 Magellan Telescope

Observations were obtained with the Baade-Magellan 6.5-m telescope at Las Campanas in Chile on 2019-02-02. This was a follow up to the observations with DCT on 2019-01-31; we needed to complete the coverage of Didymos' primary lightcurve with the additional observations to obtain a robust lightcurve decomposition on this epoch. We used the WB4800-7800 very broad band *VR* filter that covers the wavelengths between 480 and 780 nm to maximize the signal-to-noise ratio of Didymos. Didymos was imaged over about 80 minutes using 120 seconds images in photometric conditions with 0.85 arcsec seeing using the IMACS imager, which has a pixel scale of 0.2 arcsec. The photometry extraction was performed using the PhotometryPipeline described in Section 2.1. Photometry was calibrated to the PS1 catalog in the r-band using stars near Didymos in the science images.

2.9 Keck Telescope

Observations were made with the Low Resolution Imaging Spectrometer (LRIS) instrument in its imaging mode using the Atmospheric Dispersion Corrector (ADC) at Keck 1 on 2021-01-14 from 11:20 to 16:09 UT. LRIS includes both a "blue" and "red" side, with simultaneous images obtained on both sides with different filters. Here we present only red-side data analysis, blue-side images are not included in this work. The LRIS R filter has an effective wavelength of 642 nm and a full-width half-maximum (FWHM) of 119 nm [5] . The R-filter images of Didymos were obtained with 120-second exposure times. Sidereal tracking was used, with the asteroid allowed to move across the field of view. The red side of LRIS has a plate scale of 0.123 arcsec/pix. Data reduction was done using the standard techniques provided in IRAF (Tody, 1986), with extraction of magnitudes using the aperture photometry apphot routines.

Four unsaturated stars in the field with Didymos with a range of brightnesses were identified in the Sloan Digital Sky Survey (SDSS; Blanton et al. 2017, Ahumada et al. 2020) and used as on-chip standards. On-chip standard stars were selected via the SDSS online Skyserver query database, which included data up through SDSS Data Release 16 (Ahumada et al. 2020). Data Release 16 is part of SDSS-IV (Blanton et al. 2017). Three of the stars were used to calculate Didymos' magnitude, the fourth (which was of brightness similar to Didymos') was used as a comparison and control. No filter transformation was calculated between the published SDSS magnitude and the Keck R filter magnitude. The average magnitude uncertainty for Didymos and the control star on an image was typically < 0.01 mag.

While 94 images were obtained, several of the later images were compromised by twilight and were rejected. In addition, close passes to stars by Didymos as it moved in the sky and occasional unluckily-placed cosmic ray strikes compromised some measurements. A total of 69 images remained for inclusion in the lightcurve, covering the period of 11:20–15:43 UT. Apertures with diameters of 12 pixels (roughly 1.5 arcsec) were used in extraction.

[5] https://www2.keck.hawaii.edu/inst/lris/filters.html

2.10 Large Binocular Telescope

We obtained observations using the Large Binocular Telescope (LBT) on 2021-01-18 and the MODS1 and MODS2 cameras each with a v and r filter, with a plate scale of 0.12 arcsec/pixel. MODS1 and MODS2 are Multi-Object Double CCD Spectrographs/Imagers. The field of view is 6×6 arcmin, and consists of an $3\text{k} \times 3\text{k}$ image. We used these images without binning. The images from MODS2 were better, so the v and the r filter images were shifted and combined into a single data set. We obtained 150 images of 60 s exposures between 08:00 and 10:58 UT. The telescope was tracking the asteroid, and slight trailing was apparent in the stars. The detector is made up of several chips with offset background levels and 1–2 bad columns at the edges. The asteroid was kept away from the edges, but the comparison stars did move from one region to another. We used the best 3 comparison stars to obtain the differential magnitudes and linked frames where the comparison stars changed. The comparison stars were at or somewhat brighter than Didymos ($V = 16.8$ to 19.3). We used the standard aperture photometry routines in IRAF with an aperture of 10 pixel radius. The sky annulus used was at a radius of 13 pixels and was 6 pixels wide, and outliers were removed using a 3-σ clipping algorithm. The formal uncertainties are 0.004 to 0.007 mag and the estimated repeatability of the data is 0.009 mag. We measured the rms value of the comparison star data over short enough time intervals that the signal was constant in order to determine the repeatability level.

2.11 Telescopio Nazionale Galileo

Telescopio Nazionale Galileo (TNG) is operated on the island of La Palma by the Centro Galileo Galilei of the INAF (Istituto Nazionale di Astrofisica) at the Spanish Observatorio del Roque de los Muchachos of the Instituto de Astrofísica de Canarias. TNG images of Didymos were obtained on 2021-01-20 with the Device Optimised for the LOw RESolution (DOLORES) instrument. The detector is a 2048×2048 E2V 4240 thinned back-illuminated, deep-depleted, Astro-BB coated CCD with a pixel size of 13.5 μm. The scale is 0.252 arcsec/pixel. The instrument was equipped with the broadband R filter of the Johnson-Cousins system.[6] Didymos was observed with the telescope tracked at half its apparent (non-sidereal) motion. More than 300 images were acquired consecutively, starting at 2021-01-20 00:15:30 UTC, with single exposure time of 60 seconds for most of the images and with 2×2 binning.

Standard dome and sky flats did not prove themselves effective in correcting the field illumination. For this reason, a "super-flat" was made by averaging the scientific images, after masking the sources with the `MAKEMASK` IRAF package, obtaining a flat field correction better than the 1% level. On each image, a preliminary WCS solution was obtained by means of the `astroquery` python module[7] from the web service Astrometry.net[8] that provided a robust blind WCS solution. Then, optimal aperture photometry was performed with the `MAG_AUTO` routine of `SExtractor` (Bertin and Arnouts, 1996), on the

[6] http://www.tng.iac.es/instruments/filters/

[7] https://astroquery.readthedocs.io/en/latest/astrometry_net/astrometry_net.html

[8] https://astrometry.net/

whole field covered by each image. The final WCS solution was obtained with `Scamp` (Bertin, 2006), comparing the preliminary WCS positions of the stars in the field with the Gaia eDR3 catalogue, and Didymos was recognized in the field by querying the JPL catalogue with the `jplhorizons` python module, [9] cross-matching the measured Didymos positions on each image with the JPL ephemerides, by means of the `Stilts` code (Taylor, 2006).

To build Didymos' lightcurve, a set of 25 bright (non-saturated) reference stars was chosen on a reference image, collected in the middle of the run, with a typical photometric uncertainty better than 0.02 mag. The maximum relative offset of the other images, because of the motion of Didymos, was on the order of ±100 pixels in both axes. The positions of the reference stars were cross-matched between the reference and the other images with the `DAOMATCH/DAOMASTER` code (Stetson, 1993), resulting in a minimum overlap of 14 stars in the worst case. `DAOMATCH/DAOMASTER` also computes the photometric offset between the reference and the other images, with a robust weighted mean that discards the outliers and delivers a catalogue where all the measurements are photometrically aligned to the catalogue of the reference image. Computed offsets were added to the Didymos individual measurements, obtaining a homogeneous lightcurve in the reference image system. After discarding several outliers (due to a contamination of the Didymos image by nearby sources, hot pixels, or other effects) we ended up with 296 data points. The robustness of our procedure was tested by choosing a few isolated stars in the field, of brightness similar to Didymos and not among the reference stars, obtaining for each of them a flat lightcurve within the uncertainties. The median of photometric errors of the individual data points calculated by `SExtractor` was 0.011 mag, but real errors were greater (see Section 3) as the noise model in `SExtractor` does not account for all noise sources. [10] Finally, the absolute calibration was obtained by selecting, among the 25 reference stars, 11 stars with good Sloan SDSS 8 *g', r'* measurements, and then transformed to Johnson R magnitudes by means of the transformations published in Lupton et al. (2005). [11] We estimate the uncertainty of the calibration to be 0.019 mag.

[9] https://astroquery.readthedocs.io/en/latest/jplhorizons/jplhorizons.html
[10] https://sextractor.readthedocs.io/en/latest/Photom.html
[11] See also https://www.sdss.org/dr12/algorithms/sdssubvritransform/

3 Lightcurve decompositions

The lightcurve of a binary asteroid consists of generally three components: the primary rotation lightcurve, the secondary rotation lightcurve, and the mutual event (orbital) lightcurve. The primary rotation lightcurve is always apparent (with observations of sufficient accuracy), while the secondary rotation lightcurve may or may not be resolved depending on the secondary-to-primary size ratio, elongation of the secondary, and accuracy of the photometric observations. When the binary asteroid is in a mutual occultation or eclipse geometry, i.e., when Earth or Sun, respectively, is close to the mutual orbit plane of the two bodies, then there are superimposed brightness attenuations due to the occultations or eclipses (collectively called 'mutual events') that occur between the two bodies as they orbit one another. For analysis and modeling of the photometric data of a binary asteroid, we decompose its lightcurve using the method of Pravec et al. (2006), which we briefly outline in the following.

The binary asteroid lightcurve outside mutual events, consisting of the two rotational lightcurves, can be represented as a linear addition of two Fourier series

$$F(t) = F_1(t) + F_2(t), \tag{1}$$

$$F_1(t) = C_1 + \sum_{k=1}^{m_1} \left[C_{1k} \cos \frac{2\pi k}{P_1}(t - t_0) + S_{1k} \sin \frac{2\pi k}{P_1}(t - t_0) \right], \tag{2}$$

$$F_2(t) = C_2 + \sum_{k=1}^{m_2} \left[C_{2k} \cos \frac{2\pi k}{P_2}(t - t_0) + S_{2k} \sin \frac{2\pi k}{P_2}(t - t_0) \right], \tag{3}$$

where $F(t)$ is the total light flux at time t, $F_j(t)$ are the light fluxes of the components at time t, C_j are the mean light fluxes of the components, C_{jk} and S_{jk} are the Fourier coefficients, P_j are the rotation lightcurve periods, t_0 is the zero-point time, and m_j are the maximum significant orders (see also Pravec et al., 2000, and references therein). (We designate quantities belonging to the primary and secondary with the indices '1' and '2', respectively.) The two constant terms add to $C_0 = C_1 + C_2$ which is fitted in analysis. We note that the two rotational lightcurves can be taken as additive in the combined binary asteroid lightcurve if the effect of mutual illumination between the two bodies is negligible. We further note that using the representations of Eqs. 2 and 3, we assume principal axis rotation for each component; non-principal axis rotation would produce a complex lightcurve. (The lightcurve of an asteroid in the state of free precession can be represented with a 2-period Fourier series (see Pravec et al., 2005), but it might not be a good representation for a more complex or chaotic rotation of the component of an unrelaxed binary asteroid system.) The maximum significant orders m_j of the fitted Fourier series are determined from the significance F-test (see, e.g., Magnusson et al. 1995). We note that the decomposition of a binary asteroid lightcurve into the primary and secondary lightcurves with Eqs. 2 and 3 is a well-constrained problem and a unique solution is obtained with photometric data of sufficient amount and quality unless the periods P_1 and P_2 are close one to each other or commensurate (which is not the case of Didymos).

Using the representation for binary asteroid rotational lightcurves above implicitly assumes that the two rotational lightcurves are constant, i.e., neither the Fourier coefficients nor the rotation lightcurve periods change with time. (The lightcurve data must be also reduced to unit geo- and heliocentric distances and to a consistent solar phase, e.g., using the H–G phase relation, to correct for the flux changing inversely proportional with the square of the distances and with the phase function. The times were reduced for light-travel time, i.e., we work in the asterocentric frame.) In reality, the rotational lightcurves are not constant as the Earth-Asteroid-Sun viewing and illumination geometry changes with time and the synodic rotational lightcurve periods are not constant due to the varying apparent angular rate of the asteroid. (The synodic-sidereal rotation period difference can be approximated using the Phase-Angle-Bisector formalism, see, e.g., Pravec et al., 1996.) However, the rotational lightcurve shape and period changes are usually small over short time intervals and so their representation with Eqs. 2 and 3 can be used if we combine lightcurve data taken on nearby nights.

As will be shown below, observable changes of the Didymos primary rotational lightcurve occurred on timescales from a couple of days to a couple of weeks (depending on specific Earth-Asteroid-Sun geometry at individual epochs). The lightcurve data taken over longer time intervals therefore had to be analysed and decomposed separately.

Changes of the synodic primary rotation period due to the changing apparent angular rate of Didymos were generally small, on an order of a few 0.0001 hr. They were entirely negligible over the short time intervals (which were not longer than a couple weeks) of the individual Didymos lightcurve decompositions presented below, and they were also small over the course of the individual apparitions (though the estimated mean synodic periods differed slightly between the individual apparitions).

In fitting the rotational lightcurve data with the Fourier series, observations taken outside mutual events are used. Data points covering mutual events are therefore masked at this stage. As the beginning and the end of a mutual event are generally sharp lightcurve features, the data points taken in mutual events can usually be easily identified and they are masked iteratively while refining the Fourier series fit in a few steps. (While the rotational lightcurves are generally smooth and therefore can be represented with the Fourier series cut at relatively low orders, the brightness attenuations caused by mutual events begin and end abruptly as the two bodies start and finish transiting one another with respect to Earth or Sun.) When we are uncertain if a particular data point near the beginning or the end of a mutual event is in or outside the event, it is usually better to be conservative and mask it as well; we typically get enough data points outside events to define the rotational lightcurves even in the case where we mask out a few more points near the beginning or the end of an event.

When combining photometric data taken with different telescopes or on different nights, which was the case for most of the Didymos data (see below), we took the data sets obtained from different telescopes or nights as being on relative magnitude scales one to each other. Though some of the data were absolutely calibrated in specific photometric systems with uncertainties of about 0.02 mag, that was generally not accurate enough for our purpose and we took

the zero points of the magnitude scales of the individual observing runs as free parameters in the Fourier series fits.

Finally, we note that the observations of Didymos taken with different telescopes or by different teams were made in a few different filters (though most of the detector+filter combinations had a peak response at red wavelengths). Combination of lightcurve data taken in different filters (at visible wavelengths) is not considered to be a problem for the lightcurve analysis, as asteroids do not show large scale color non-uniformities, so the lightcurves measured in different filters are expected to look the same. Nevertheless, in the lightcurve decompositions presented below we paid attention to possible systematic differences between data from different telescopes that might be attributable to a large scale color difference, but we did not find any.

Table 2: Didymos lightcurve decompositions

Sessions	Points	Events	Rms res. (mag)	α (°)	ν (°)	Plot
2003-11-20.9 to 2003-11-24.3	1111	5	0.008	15.4	27.0	P06 (Fig. 1)
2003-11-26.2 to 2003-12-04.1	778	8	0.008	4.8	34.9	P06 (Fig. 2)
2003-12-16.9 to 2003-12-20.3	458	5	0.012	8.3	52.7	P06 (Fig. 3)
2015-04-13.3 to 2015-04-14.4	120	2	0.024	3.1	168.2	Fig. 1
2017-02-23.3 to 2017-03-01.3	304	2	0.017	17.9	146.9	Fig. 2
2017-03-31.1 to 2017-04-02.3	144	2	0.025	3.8	155.7	Fig. 3
2017-04-18.2 to 2017-05-04.3	233	3	0.030	16.3	161.9	Fig. 4
2019-01-31.4 to 2019-02-02.2	119	2	0.011	25.7	126.7	Fig. 5
2019-03-09.1 to 2019-03-11.1	374	3	0.010	4.1	138.7	Fig. 6
2020-12-12.6 to 2020-12-23.4	333	4	0.011	44.2	87.9	Fig. 7
2021-01-08.5 to 2021-01-10.4	289	6	0.010	33.3	100.5	Fig. 8
2021-01-12.6 to 2021-01-14.6	283	4	0.008	30.7	102.6	Fig. 9
2021-01-17.5 to 2021-01-18.4	292	4	0.006	27.8	104.7	Fig. 10
2021-01-20.2	296	2	0.015	26.2	105.8	Fig. 11
2021-02-17.4	121	2	0.012	5.2	118.0	Fig. 12
2021-03-06.3	149	1	0.011	11.1	124.5	Fig. 13

Note: P06 is Pravec et al. (2006).

We applied the lightcurve decomposition method outlined above to the obtained Didymos photometric data from the five apparitions presented in Section 2. We present the lightcurve decompositions data in Table 2 and in the figures referenced there. We have obtained the lightcurve decompositions for data taken during 16 separate intervals (including the three presented in

Pravec et al., 2006), with the primary rotation lightcurve shape appearing constant during each of the individual intervals. In the table, the first column gives the observational interval used for the individual decomposition, with the subsequent columns giving the total number of photometric data points used, the number of events covered (at least partially) by the observations, the rms residual of the best Fourier series fit to the rotational lightcurve data outside events (it was converted from light flux units to magnitudes using $\delta m = 2.5\delta F/C_0/\ln 10$), the solar phase angle (α), the true anomaly of Didymos in its heliocentric orbit (ν; these two angles are for the center of the given observational interval) and the reference to a plot of the lightcurve decomposition. We note that though we did the fits of the Fourier series (Eqs. 2 and 3) in light flux units, i.e., we converted the reduced magnitudes to flux units for the fitting, we then converted the resulting separated lightcurve components back to magnitudes for plotting in panels b and c of the presented figures. (The individual lightcurve components plotted in panels b and c of the figures were obtained from the reduced photometric data by subtracting the variable parts of the other lightcurve components (Eqs. 2 and 3). The constant part $C_0 = C_1 + C_2$ was kept and it was not subtracted for the plotting. This is because we do not know *a priori*, before further modeling that follows the lightcurve decomposition, what fraction of the mean light flux of the system (C_0) belongs to the primary or to the secondary.) These plots show how the Didymos lightcurve would appear if there was only the secondary/orbital lightcurve present (panel b; corresponding to a case of spheroidal primary) or only the primary lightcurve present (panel c; corresponding to a case of spheroidal secondary and the system being outside mutual event geometry). In the figures, the solid curves are the fitted Fourier series (Eq. 1) in panels a, and the fitted primary rotational lightcurve (Eq. 2, with the constant part C_0 kept, as commented above) in panels c. **The Fourier series coefficients are presented in Appendix A.** We comment on the individual lightcurve decompositions presented in Table 2 and the figures referenced there in the following.

The Didymos photometric data taken in 2003 were analyzed and their lightcurve decompositions were presented in Pravec et al. (2006). The three lightcurve decompositions obtained covered intervals 4, 8 and 4 days long; see the first three rows in Table 2. They were high-quality data with the rms residuals of the Fourier fits to the rotational lightcurve components of 0.008, 0.008 and 0.012 mag, respectively. As many as 18 mutual events were fully or partially covered by the observations. The shapes of the mutual events changed quite rapidly with the changing Earth-Asteroid-Sun geometry during the observations taken shortly after the close approach to Earth that occurred on 2003 November 12. The changes were particularly prominent for the primary events (plotted around orbital phase 0.25 in Figs. 1b to 3b of Pravec et al., 2006) as they were particularly sensitive to specific viewing and illumination geometry of the binary system in the observed primary eclipses and occultations. We also note that the observed synodic primary rotation period was 2.2592-2.2593 h and so this value was used for the lightcurve decompositions of the 2003 data, but the synodic-sidereal primary rotation period difference was estimated to be 0.0008 h; the sidereal primary rotation period was determined to be 2.2600 ± 0.0001 h in further modeling (see Naidu et al., 2020). We further note that the synodic orbital period was estimated to be 11.91 h and it was used for the lightcurve decompositions. (Again, the sidereal orbital period was slightly greater, see Scheirich and Pravec, 2022.) Our last comment on the

2003 data is that the data obtained after subtraction of the primary lightcurve component did not show a flat (constant) secondary lightcurve outside mutual events (see Figs. 1b to 3b of Pravec et al., 2006). While Pravec et al. (2006) suggested that it might be due to rotation of a non-spheroidal secondary, we consider the features seen in the 2003 secondary lightcurves outside mutual events to be spurious rather than real features produced by the secondary's rotation (see Section 4).

The observations taken with DCT on 2015-04-13 and 14 were quite limited (total coverage of 7.4 h) and relatively noisy, but we were able to decompose them (Fig. 1). For the lightcurve decomposition, we assumed the synodic periods observed in 2003. (Possible small differences between actual synodic periods in April 2015 and those observed in 2003 would be entirely negligible for decomposition of the short 2015 data.) As for the decompositions of the 2003 data in Pravec et al. (2006), we used $G = 0.20$ by Kitazato et al. (2004) for reduction of the 2015 data (as well as the 2017-2021 data below) with the H–G phase relation. Despite the relatively high noise of the 2015 data (their rms residual was 0.024 mag), we detected nearly all of one mutual event and a small part of another event (see Fig. 1b). The primary lightcurve (Fig. 1c) was quite complex with several local extrema; the harmonics up to the 8th were significant ($m_1 = 8$ in Eq. 2). This multi-modal primary lightcurve, which is markedly different from the primary lightcurves observed in 2003 (Figs. 1c to 3c in Pravec et al., 2006) that were predominated by the 1st or 2nd harmonic, indicates that there were local topography effects present at the viewing and illumination aspect in April 2015 that were not seen in 2003. (The 2015 observations were taken at a small solar phase angle of 3° so the observed multimodal primary lightcurve shape was not related to a complex shadowing that could be present at high phase angles.) These data may be useful for refining the primary shape model in future.

In 2017 we obtained 3 lightcurve decompositions (Figs. 2 to 4). They were mostly relatively noisy data again (rms residuals 0.017 to 0.030 mag), but we were able to decompose them grouped in three intervals that were 6, 2 and 16 days long. (The last interval might seem somewhat long, but we did not see an obvious change of the primary lightcurve shape over the 16 days, though it is possible that small changes of the primary lightcurve shape were hidden in the noise.) Despite the noise, we detected 7 mutual events in full or partially. Like in April 2015, the primary lightcurves (Figs. 2c to 4c) showed multiple extrema. This indicates that the features of local topography that affected the 2015 primary lightcurve were present during the 2017 observations as well. Indeed, the heliocentric true anomaly of Didymos during the 2017 observations, 147°–162°, was similar to its true anomaly on 2015 April 13-14 (168°) —Didymos was seen on similar aspects in the two apparitions—, but it was quite different from the true anomaly values 27°–53° of the 2003 observations when we saw the more regular primary lightcurves. We note that we found that the synodic primary period in this apparition was close to (within error bars of) the 2.2600-h sidereal primary period, so, we used this period for the 2017 lightcurve decompositions. We estimated that the synodic orbital period was 11.917 h in this apparition; like in 2003, it was somewhat shorter than the sidereal orbital period we found in subsequent Dimorphos orbit modeling.

In 2019 we obtained 2 lightcurve decompositions (Figs. 5 and 6). Unlike the

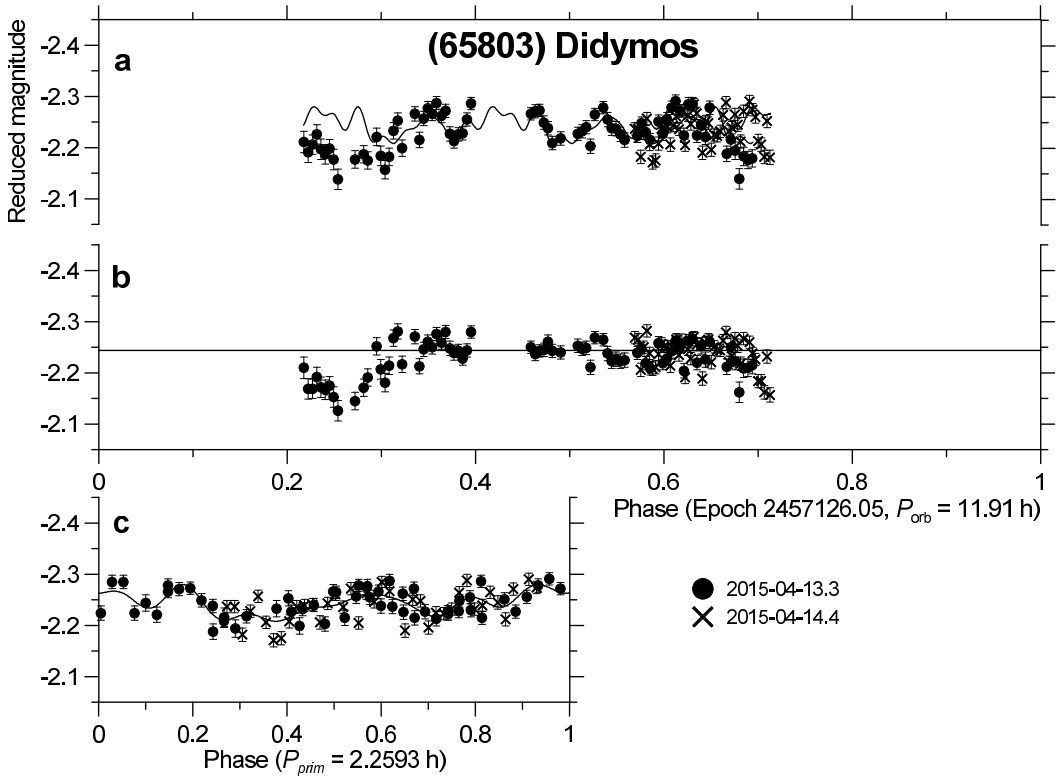

Fig. 1. Didymos lightcurve from 2015-04-13 to 2015-04-14. (a) The data showing all lightcurve components, folded with the synodic orbital period. (b) The secondary (orbital) lightcurve component, derived after subtraction of the primary lightcurve component, showing the mutual events between the components of the binary system. **The horizontal line indicates the mean level outside mutual events (corresponding to C_0).** (c) The primary lightcurve component.

2015 and 2017 data, the 2019 data were of high quality (we made observing strategy improvements based on experience obtained in 2015 and 2017) with rms residuals of 0.010–0.011 mag. We detected 5 mutual events partially or in full. We found that the synodic primary and orbital periods in 2019 were close to the values observed in 2017, though we were not able to refine them with the short 2019 intervals (both only 2 days long); we used the 2017 synodic period values for the 2019 lightcurve decompositions. It is notable that the primary lightcurves observed in this apparition (Figs. 5c and 6c) were regular again, similar to those observed in late November and December 2003. Apparently the local topography features that caused the complex multimodal primary lightcurves in 2015 and 2017 did not affect it in 2019 when Didymos was seen at lower heliocentric true anomaly values 127°–139°. We further note that the GTC observations of 2019-03-09 to 11 showed a non-constant secondary lightcurve outside events; it will be analyzed in Section 4.

The rich data we took in the 2020–2021 apparition allowed us to obtain as many as 7 lightcurve decompositions (Figs. 7 to 13). They were high quality data with the rms residuals from 0.006 to 0.015 mag. We detected 23 mutual events partially or in full. The synodic primary period was 2.2602 h (formal error < 0.0001 h) as we determined from the highest quality data obtained from 2020-12-12 to 2021-01-18 and we used this value for all the lightcurve decompositions in this apparition. The synodic orbital period was close to the 11.917-h value observed in 2017 and we used it for all the 2020–2021 lightcurve decompositions. It is particularly interesting that the mutual

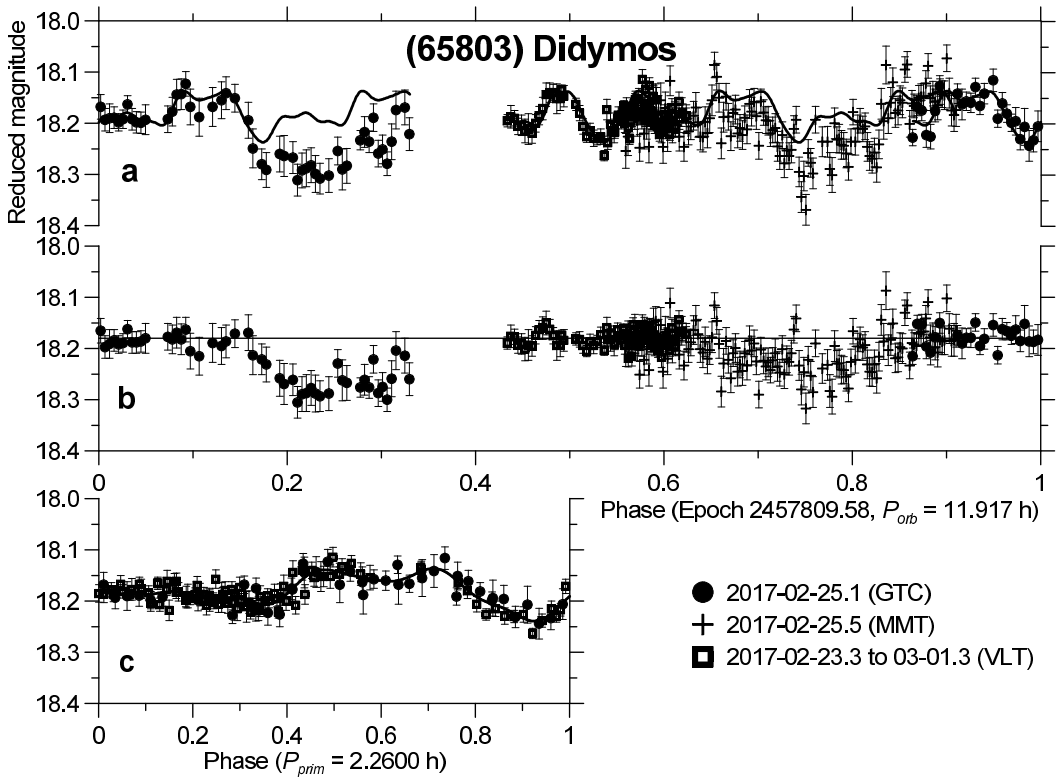

Fig. 2. Didymos lightcurve from 2017-02-23 to 2017-03-01. See caption of Fig. 1 for description of the content of the panels.

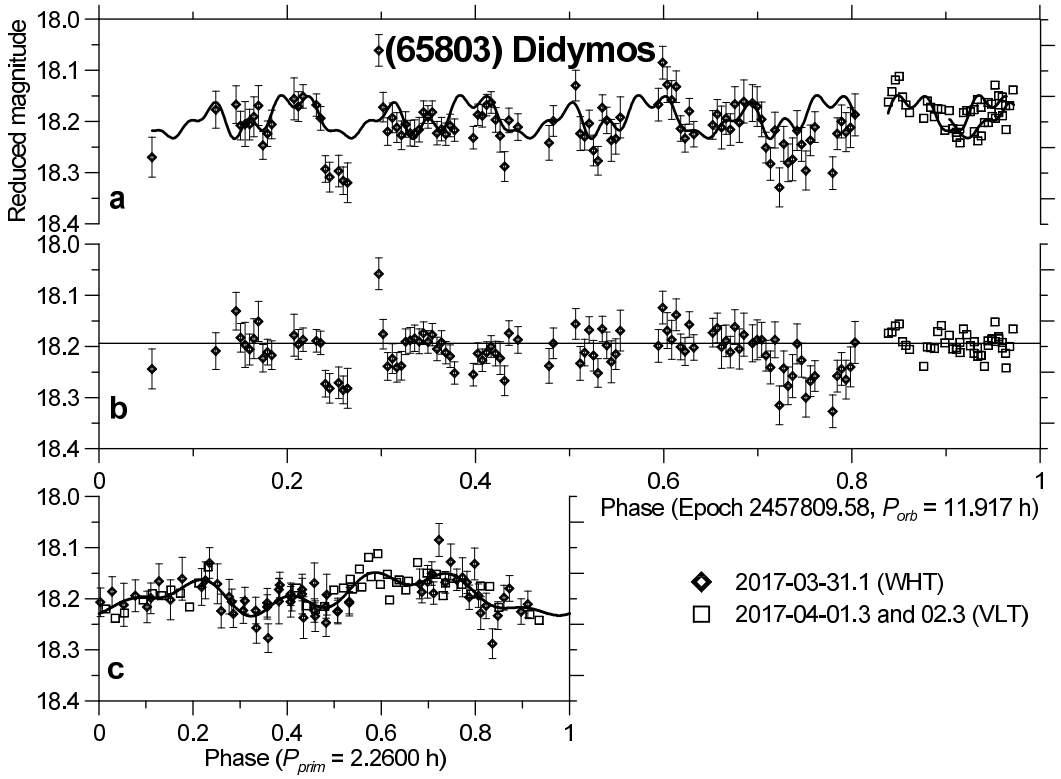

Fig. 3. Didymos lightcurve from 2017-03-31 to 2017-04-02. See caption of Fig. 1 for description of the content of the panels.

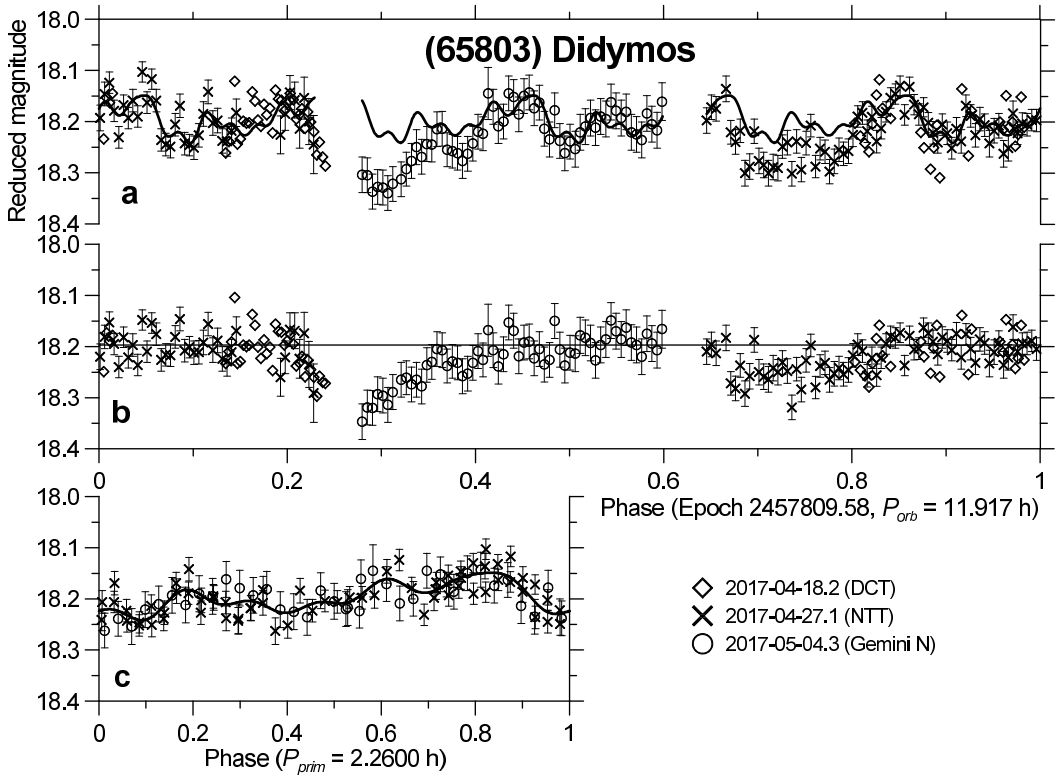

Fig. 4. Didymos lightcurve from 2017-04-18 to 2017-05-04. See caption of Fig. 1 for description of the content of the panels.

events were less prominent, mostly shorter and shallower, in this apparition than in all the previous four observed apparitions. This was apparent especially between 2021-01-08 and 18 (Figs. 8b to 10b) when the primary eclipses, observed around orbital phase 0.29, were short and relatively shallow (with depths about 0.04 mag) and the primary occultations (we have identified the character of the individual events in Scheirich and Pravec, 2022), observed around orbital phase 0.21, were even shallower, especially during January 8–14 when their depth was as low as 0.019 mag (cf. with the depth of the total secondary events 0.050 ± 0.002 mag observed on other epochs, see Scheirich and Pravec, 2022). Apparently the Didymos binary system was seen significantly off the mutual orbit plane, i.e., at relatively high angles between its mutual orbit plane and the Asteroid-Earth/Sun line (we call them 'aspect angles') that caused the observed occultations/eclipses to be quite off-center and partial. Indeed, as Scheirich and Pravec (2022) found, both aspect angles were near their maximum values in January 2021, while at least one of them was not close to the extreme on any other epoch in all the five observed apparitions. As for the primary lightcurves (Figs. 7c to 13c), they showed multiple extrema in December 2020 and January 2021 again, but it might be a result of observing Didymos at relatively high solar phases (26°–44°), where effects of local topography could be more prominent.

We conclude this section with stating that the photometric data set we obtained for Didymos in the five apparitions during 2003–2021 is among the best obtained for binary near-Earth asteroids so far (comparable only to the data obtained for (66391) 1999 KW4 and (175706) 1996 FG3). Despite the relatively small size of the Didymos secondary ($D_2/D_1 = 0.21$; Scheirich and Pravec, 2009), resulting in relatively shallow mutual events, we obtained high quality

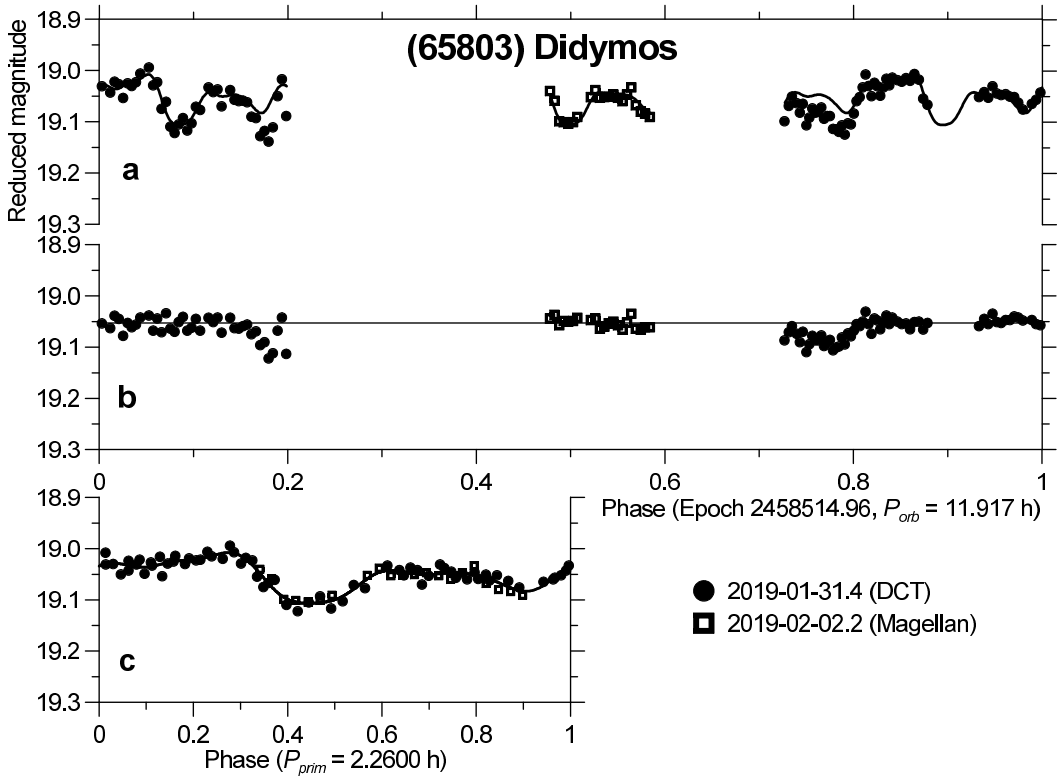

Fig. 5. Didymos lightcurve from 2019-01-31 to 2019-02-02. See caption of Fig. 1 for description of the content of the panels. Note: In this and subsequent figures showing the high-quality data from 2019 and 2020-2021 with errors around 0.01 mag, we do not plot error bars for the individual data points as they are comparable to the sizes of the data point symbols.

data for a good number of mutual events. This required the use of medium- to large-sized telescopes as Didymos was relatively distant and therefore rather faint during 2015–2021. The obtained mutual event data have been used for modeling the Dimorphos orbit (Scheirich and Pravec, 2022; Naidu et al., 2022). The rich experience we have obtained through these observations over five apparitions will be used for performing further high-quality observations before and after the DART impact in the 2022–2023 apparition of Didymos.

4 Constraints on the Dimorphos equatorial elongation

One of the most important parameters of a binary asteroid that can be estimated or constrained from lightcurve analysis is an equatorial axis ratio (a_2/b_2) of the secondary. Information on the parameter is contained in the amplitude of the secondary lightcurve component (Eq. 3). Pravec et al. (2016) analysed secondary lightcurve data for 46 near-Earth and small main-belt asteroids and found that the secondary equatorial elongations have an upper limit of a_2/b_2 of about 1.5. Following this constraint, the DART team has assumed $a_2/b_2 = 1.3 \pm 0.2$ for Dimorphos. Our preliminary analyses of the Didymos secondary lightcurve data in the past years revealed that estimating Dimorphos' equatorial elongation is challenging. This has been because, unlike most binary asteroid secondaries studied in Pravec et al. (2016), the Didymos

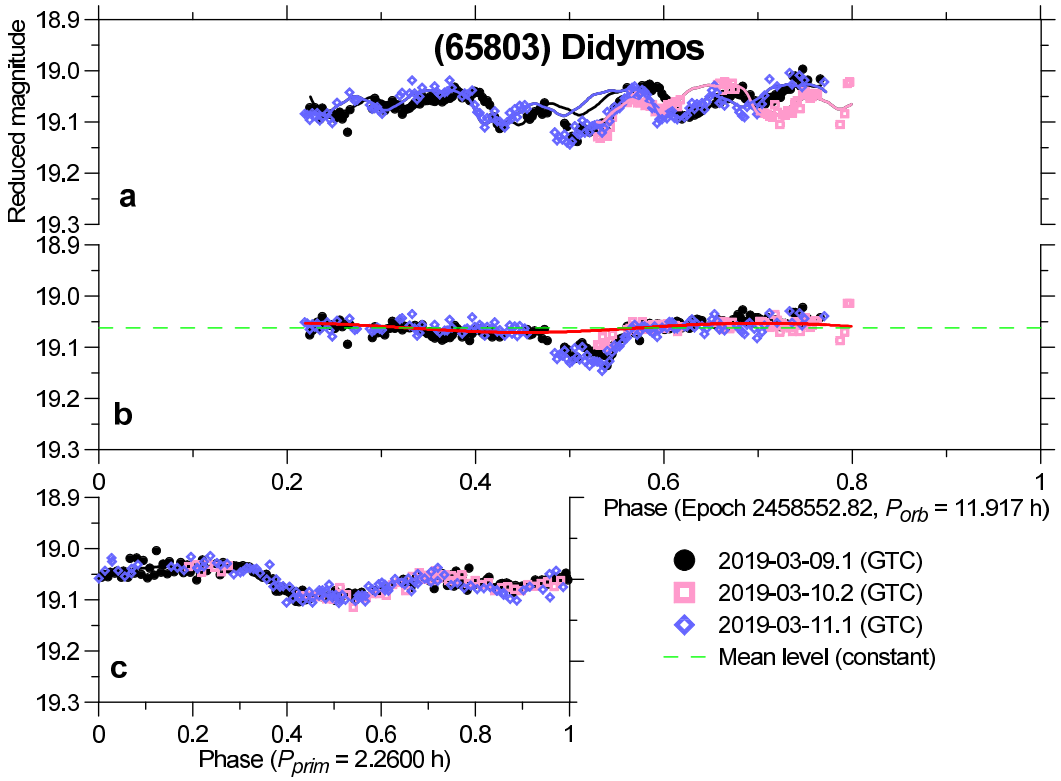

Fig. 6. Didymos lightcurve from 2019-03-09 to 2019-03-11. See caption of Fig. 1 for description of the content of the panels. **The data points from the individual nights and the Fourier series (Eq. 1) fitted to them (outside mutual events) are color-coded in this plot (as well as in following Figs. 7 to 10); this is to facilitate seeing the quality of the fit to the data outside events in panel a where the data from different nights phased with the orbit period heavily overlap.** The red curve is the best fit secondary lightcurve, see Section 4. Note that the zero point time (epoch) for this plot was arbitrarily shifted by −0.25 in orbital phase —the observed secondary events are plotted around orbital phase 0.50 and not 0.75 as in all the other plots— to show the secondary lightcurve variation (outside of mutual events) on one continuous plot; it would break at orbital phase 1.0 if we plotted the events around phase 0.75.

secondary is relatively small ($D_2/D_1 = 0.21$) and so the signal from its rotation is diluted in the light of the much larger primary.[12] That, together with the fact that the observations of Didymos in 2015–2021 were largely optimized for the DART mission-critical task of precisely determining Dimorphos' orbit around the primary and not for estimating its elongation, resulted in not yet achieving a conclusive result on Dimorphos' a_2/b_2. In this section, we analyze the available data and define requirements for potential observations optimized for estimating Dimorphos' elongation in July–September 2022 (before the DART impact).

Pravec et al. (2006) found that their derived Didymos secondary lightcurve components were not flat (constant) at orbital phases outside mutual events (see their Figs. 1b to 3b). They suggested that the variations seen outside the mutual events might be due to rotation of a non-spheroidal secondary.

[12] Unlike the case of the binary asteroid secondary, we note that estimating equatorial elongations of single asteroids with magnitudes similar to Didymos, $V = 19$–20, from photometric observations is a routine task (e.g., Thirouin et al. 2018).

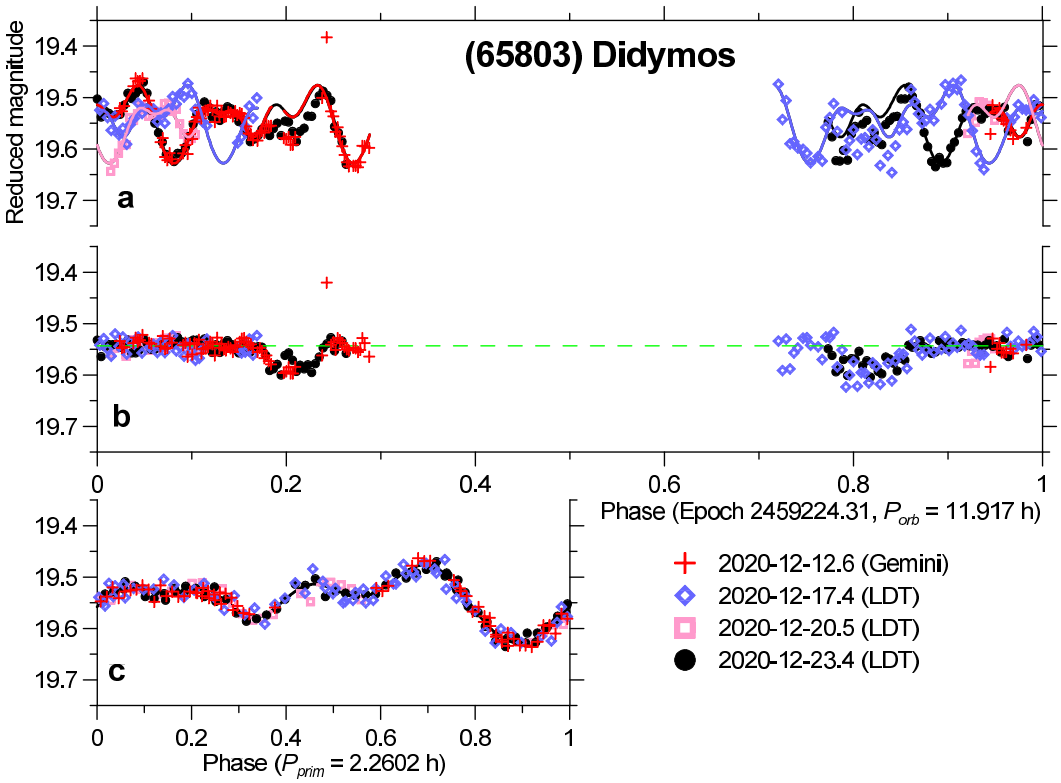

Fig. 7. Didymos lightcurve from 2020-12-12 to 2020-12-23. See caption of Fig. 1 for description of the content of the panels.

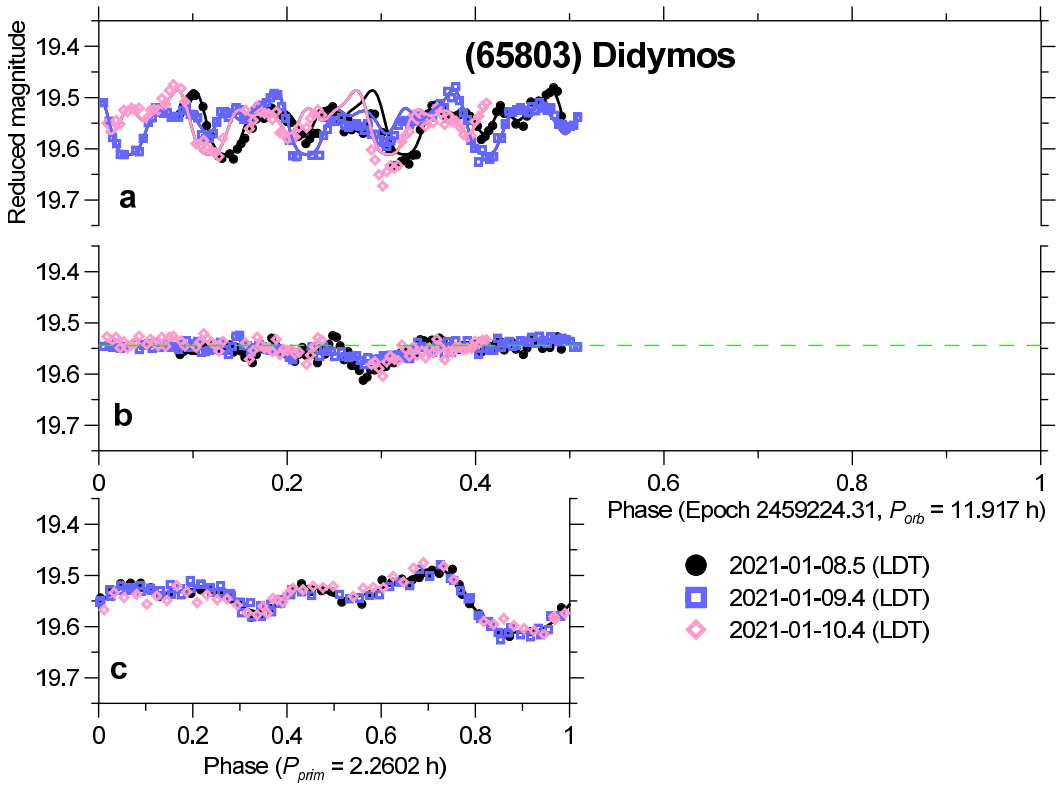

Fig. 8. Didymos lightcurve from 2021-01-08 to 2021-01-10. See caption of Fig. 1 for description of the content of the panels.

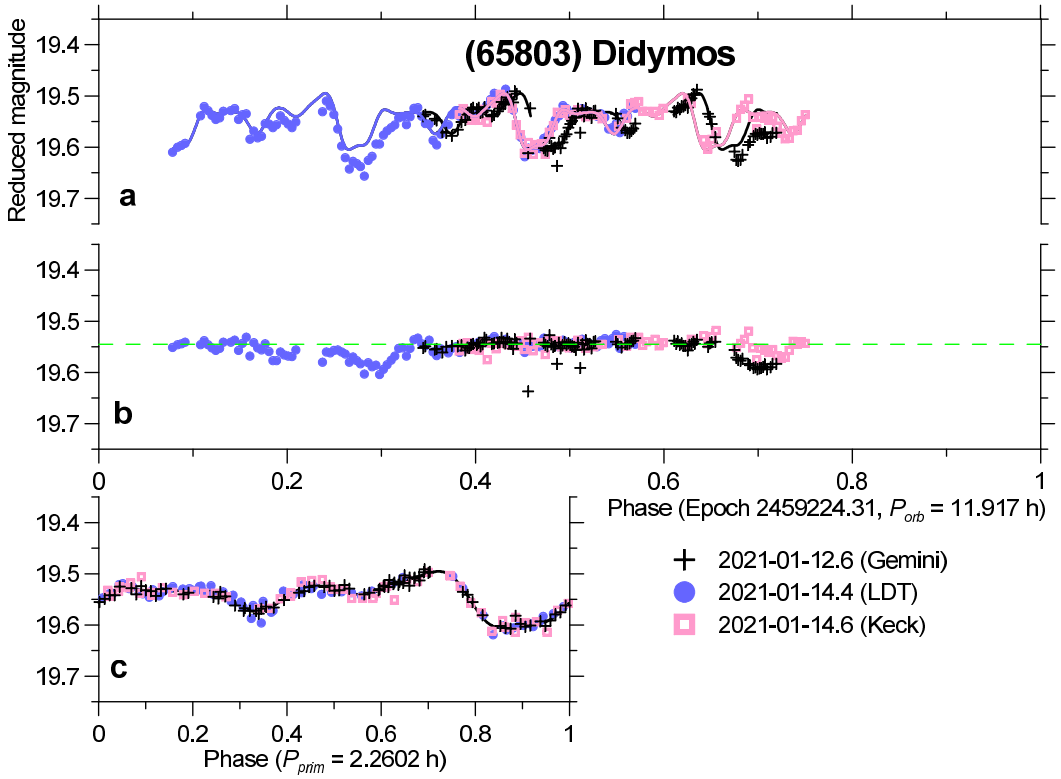

Fig. 9. Didymos lightcurve from 2021-01-12 to 2021-01-14. See caption of Fig. 1 for description of the content of the panels.

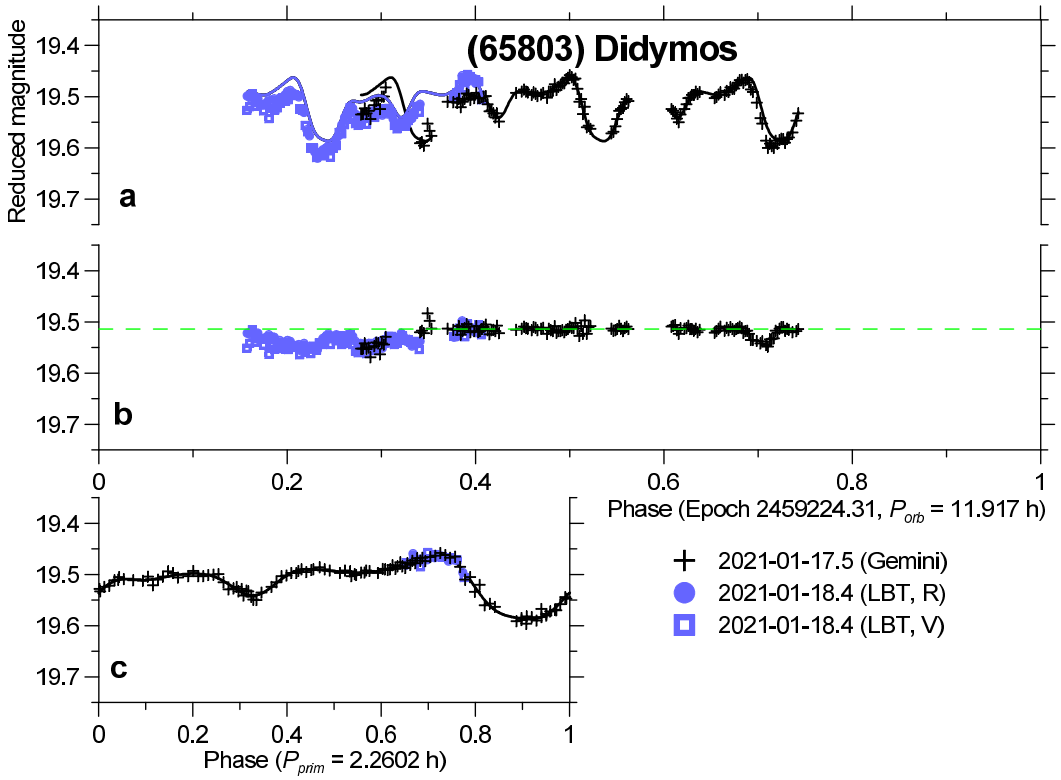

Fig. 10. Didymos lightcurve from 2021-01-17 to 2021-01-18. See caption of Fig. 1 for description of the content of the panels.

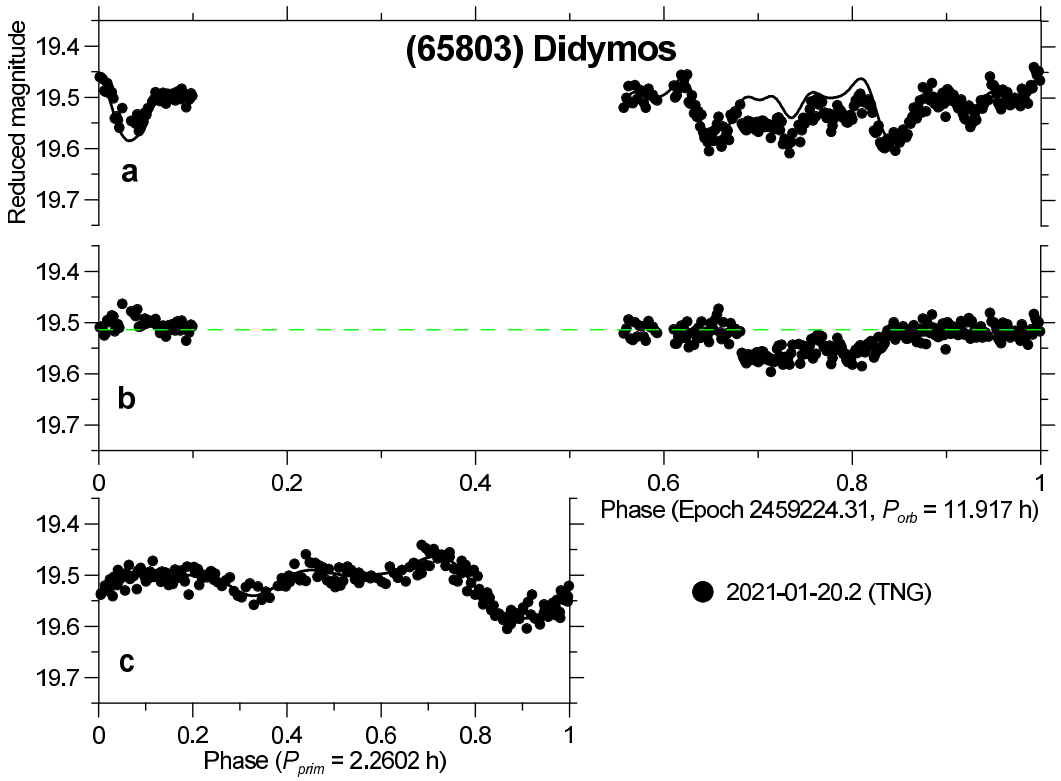

Fig. 11. Didymos lightcurve from 2021-01-20. See caption of Fig. 1 for description of the content of the panels.

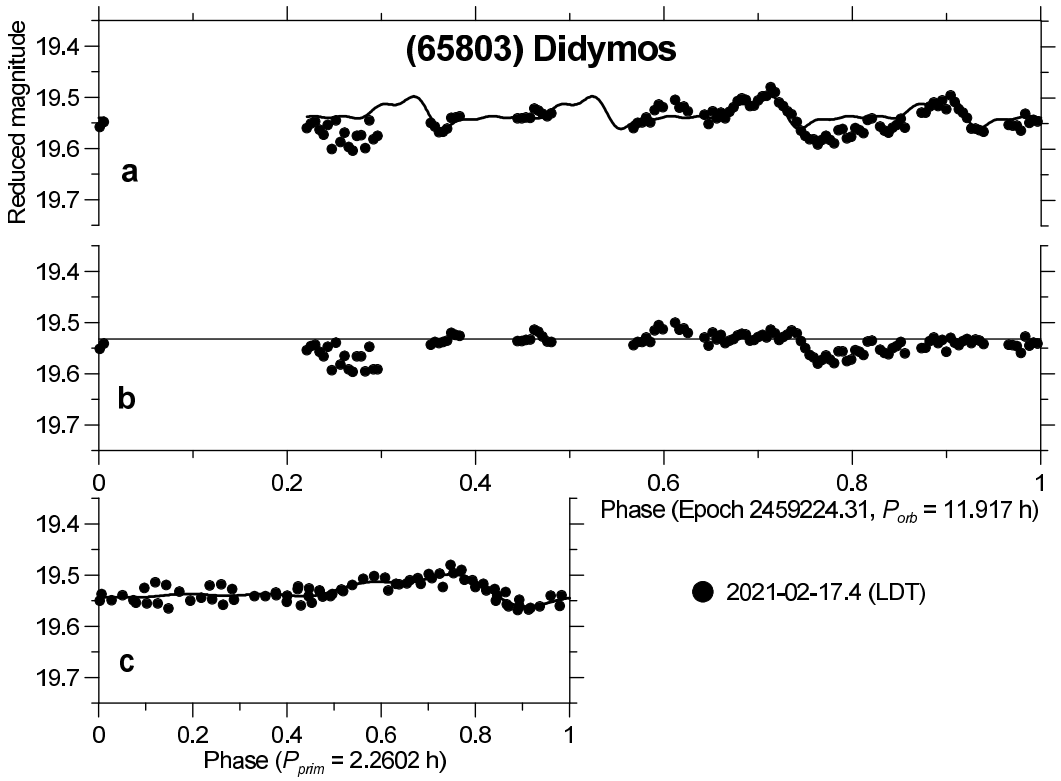

Fig. 12. Didymos lightcurve from 2021-02-17. See caption of Fig. 1 for description of the content of the panels.

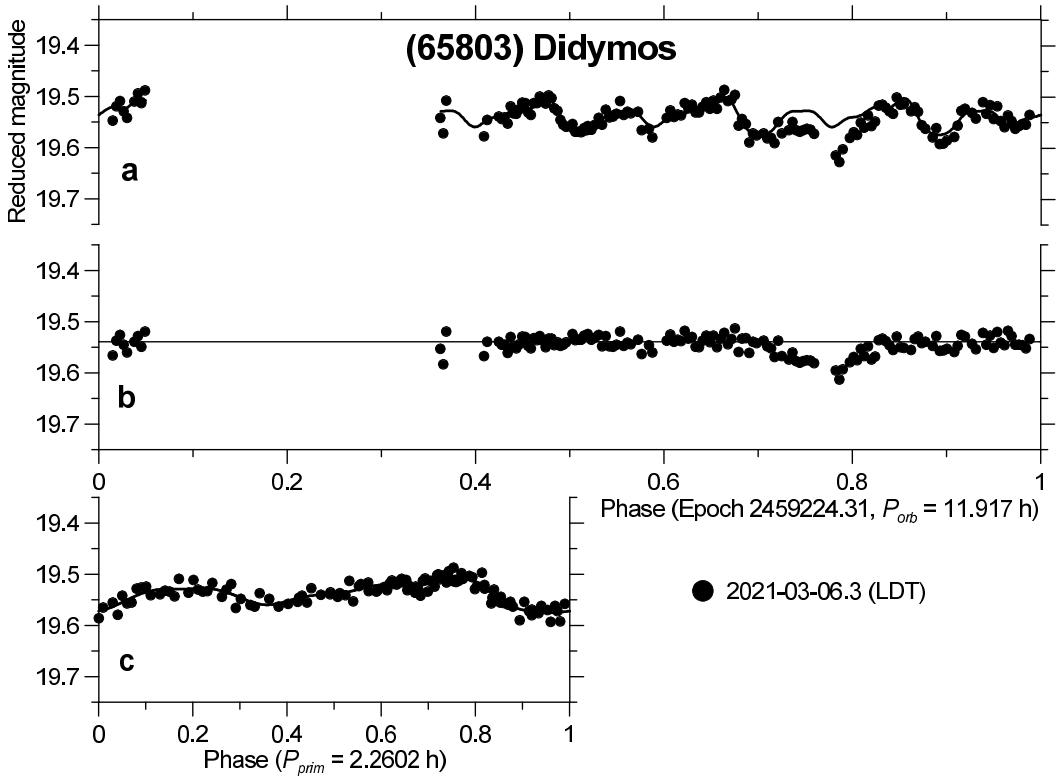

Fig. 13. Didymos lightcurve from 2021-03-06. See caption of Fig. 1 for description of the content of the panels.

However, upon further examination of their observations, following more experience that we obtained with observations of binary asteroids since 2006, we more recently suspect that the features seen in the derived 2003 secondary lightcurves outside mutual events are spurious. We suspect that the apparent variations might be artifacts caused by certain observational issues (such as imperfect flatfields) which they did not have under full control for the fast moving target in 2003. This suspicion has been strengthened because the apparent features did not look like a rotational lightcurve of a synchronous secondary (we note that Dimorphos is expected to be in the 1:1 synchronous spin state, as are the secondaries of other well-observed binary asteroids with parameters similar to the Didymos system; Pravec et al., 2016) and they did not repeat consistently over the three observational intervals. Therefore we suggested that a rotational lightcurve of the Didymos secondary could be detected with future high-quality observations that would provide photometry consistent at a 0.01-mag (or better) level over several hours covering at least a half of the mutual orbit period. This data-quality requirement was set based on the experience obtained with photometry of other binary asteroids with parameters similar to Didymos (Pravec et al., 2016). In particular, a moderately elongated secondary with $D_2/D_1 = 0.21$ would produce a secondary lightcurve amplitude in the combined primary plus secondary lightcurve data not greater than 0.02 mag, hence the need to obtain data consistent at the 0.01-mag level or better.

The photometric observations that we performed in 2015–2021 were mostly of insufficient photometric accuracy or coverage for detecting a rotational lightcurve of Dimorphos. However, there were a few high quality and suffi-

ciently long observational runs that allowed us to analyze possible secondary rotational variations outside mutual events.

The data obtained with the LDT on 2019-01-31, 2020-12-23, 2021-01-14 and 2021-03-06, with the third run supplemented with the Keck R data of 2021-01-14, were of both high quality (errors about 0.010 mag) and consistent photometric coverage with durations ≥ 5.6 h (i.e., about half of the orbit period), thus suitable for analysis of a possible secondary rotational variation outside mutual events. **To check for its possible presence,** we fitted the data with the Fourier series (Eq. 3) with the period P_2 set to half of the orbit period and $m_2 = 1$. This setting is because the rotational lightcurve of an elongated synchronous secondary is expected to be predominated by the 2nd harmonic of the orbit period, which corresponds to the 1st harmonic of half of the orbit period (see Pravec et al., 2016). We found no significant secondary rotational lightcurve amplitude in the first, second and fourth run; the F-test gave 0.5, 1.1 and 1.6 for them, respectively. The formal 3-σ upper limits on the secondary amplitudes in the three runs were 0.013, 0.009 and 0.011 mag, respectively. (We follow the convention in the asteroid research field and report "peak-to-trough" amplitudes of the asteroid lightcurves.) There was a marginal signal in the secondary lightcurve of the LDT+Keck run 2021-01-14; the F-test gave 3.5 for it with the secondary lightcurve amplitude $A_2 = 0.007$ mag with a formal error of ± 0.002 mag. Correcting for the mean light from the primary using the formulas in Pravec et al. (2006) gives an estimate for the secondary's equatorial elongation $a_2/b_2 = 1.15$ with a formal error of ± 0.05. As the observations were taken at a solar phase angle of 30° where the secondary lightcurve amplitude could be affected by the amplitude-phase effect (Zappalà et al., 1990), it might need to be corrected for that. Using the correction method of Pravec and Harris (2007), we obtained a corrected $a_2/b_2 = 1.09$. However, given that we are not sure how exactly the amplitude-phase effect works in the binary asteroid secondary, we suggest to adopt the mean of these two values, i.e., $a_2/b_2 = 1.12$. Alternatively, it might be perhaps better to say that we have estimated a formal 3-σ upper limit on the Dimorphos equatorial axis ratio of 1.30. However, as this exercise was all about analysing a signal buried in statistical noise of the observations, we can not be certain that there were no hidden systematic errors present in the LDT+Keck data on the level of a few 0.001 mag, so, we must consider the possibility that there might be some systematic error present in the a_2/b_2 estimate, though we cannot estimate its magnitude at the current stage of our work on the data.

The observations taken with GTC on 2019-03-09, 10 and 11 showed, however, a different behavior. A formally significant period of 6.05 h (formal error ± 0.03 h) for a monomodal lightcurve was detected, which corresponds to a bimodal (i.e., predominated by the 2nd harmonic as expected for an elongated secondary, see above) secondary rotational lightcurve with a period of 12.10 h with a formal error of ± 0.06 h. This is close but not exactly equal to the Dimorphos' orbital period of 11.92 h. Assuming that the difference between the two periods of 0.18 h is not significant (the P_2 formal error of 0.06 h might be underestimated), we obtained a secondary lightcurve amplitude of $A_2 = 0.017$ mag with a formal error of ± 0.001 mag assuming $P_2 = P_{\rm orb} = 11.92$ h. With the methods mentioned in the previous paragraph, this gave an estimate for $a_2/b_2 = 1.41$ or 1.37 (the latter after correcting the data for the amplitude-phase effect) with a formal error of ± 0.05; for the reasons mentioned above, we would adopt $a_2/b_2 = 1.39$. This is markedly different from the estimate

$a_2/b_2 \approx 1.12$ obtained from the 2021-01-14 LDT+Keck data.[13] Though the formal 3-σ error bars of the GTC and LDT+Keck estimates overlap (the true a_2/b_2 might thus be perhaps in the range 1.22–1.30), we feel that it is premature to accept any of the a_2/b_2 estimates that are based on these limited data. In particular, we must consider that the GTC data might be affected by a systematic error over the ~ 6.5 h long observational runs on the 2019-03-09 and 11 nights. As described in Section 2.3, the asteroid transited over the entire field of view of the GTC's OSIRIS camera during the 6.5-h run, so any systematic errors present, e.g., in the flatfield correction on the order of $\sim 1.5\%$, might produce an artificial secondary signal with a period close to 24/4 h. The apparent secondary lightcurve period 6.05 ± 0.03 h might then be not a detection of a real secondary rotation period (or its half), but an observational artifact repeating with the integer fraction of Earth's rotation period for the observations taken from one station and during the same UT hour intervals on nearby nights. Though we do not have any direct evidence for or against the presence of this or other systematic errors in the GTC observations, we have to be cautious and require a confirmation of the suggested a_2/b_2 estimates.

We conclude that the photometric observations obtained so far have not yet brought a trustworthy estimate for Dimorphos' equatorial axis ratio. The signal from the secondary rotation is diluted in the light of the much larger primary and its amplitude in the combined primary+secondary lightcurve is comparable to or lower than the photometric errors of the observations obtained during 2003–2021. To reveal Dimorphos' rotational lightcurve and to estimate its equatorial elongation with a good degree of confidence, we will need to take very high quality observations with photometric errors, both random and systematic, of 0.005 mag or less. Taking such observations over at least half of Dimorphos' orbital period on at least two nights and with at least two different telescopes will probably be needed to obtain confidence in the results for the secondary lightcurve, by seeing a mutual consistency between the obtained data. While getting data with statistical errors of 0.005 mag will not be a problem with good telescopes when Didymos is bright ($V = 14.5$–18) in July-September 2022, it may be particularly demanding to control all potential systematic error sources to within 0.005 mag for the (relatively) fast moving target over a 6-h long nightly observing run.

5 Conclusions

The photometric observations performed for the Didymos binary asteroid system with 11 telescopes with diameters from 3.5 to 10.4 m in 2015–2021 provided detections of as many as 37 mutual occultation/eclipse events between the binary system components. The full photometric data set containing 55

[13] The large difference between the apparent secondary amplitudes seen on 2019-03-09 to 11 and 2021-01-14 could not be caused by a difference in viewing geometry as the secondary was seen, assuming its spin pole is the same as the mutual orbit pole, at nearly same aspect on both epochs. For the mutual orbit pole solution by Scheirich and Pravec (2022), the angle between the Earth-Asteroid line and the Dimorphos equatorial plane was 16.4° and 16.8° , respectively, on the two epochs.

mutual events, including the 18 detected in 2003 (Pravec et al., 2006), provides a great basis for modeling Dimorphos' orbit around the primary (Scheirich and Pravec, 2022; Naidu et al., 2022). The decomposed primary lightcurve data, which reveal a complex primary lightcurve shape on some epochs, may be useful for refined primary shape modeling when combined with the 2003 radar and lightcurve observations in the future. Detection of the secondary rotational lightcurve turned out to be challenging due to the relatively small size of Dimorphos, with first estimates on the Dimorphos equatorial axis ratio being mutually inconsistent. The observational requirements for obtaining a successful detection of the Dimorphos rotational lightcurve are given. These observations will be challenging, but potentially doable when Didymos is bright in July-September 2022.

Acknowledgements

The work by P. Pravec and P. Scheirich was supported by the Grant Agency of the Czech Republic, Grant 20-04431S. N. Moskovitz and A. Thirouin acknowledge support from NASA NEOO grants NNX14AN82G and NNX17AH06G, awarded to the Mission Accessible Near-Earth Object Survey (MANOS). J. de León and J. Licandro acknowledge financial support from the NEO-MAPP project, under grant agreement No. 870377. These results made use of the Lowell Discovery Telescope (LDT) at Lowell Observatory. Lowell is a private, non-profit institution dedicated to astrophysical research and public appreciation of astronomy and operates the LDT in partnership with Boston University, the University of Maryland, the University of Toledo, Northern Arizona University and Yale University. The Large Monolithic Imager was built by Lowell Observatory using funds provided by the National Science Foundation (AST-1005313). Based in part on observations collected at the European Southern Observatory under ESO programmes 098.C-0793, 099.C-0075 and 0103.C-0282. Based in part on observations made with the Gran Telescopio Canarias, installed in the Spanish Observatorio del Roque de los Muchachos of the Instituto de Astrofísica de Canarias, in the island of La Palma, under programs GTC39/16B and GTC25/19A. The William Herschel Telescope is operated on the island of La Palma by the Isaac Newton Group of Telescopes in the Spanish Observatorio del Roque de los Muchachos of the Instituto de Astrofísica de Canarias. WHT photometry was made through programme W/2017A/02. Based in part on observations obtained at the international Gemini Observatory (with Program IDs: GN-2017A-FT-16, GN-2019A-FT-105, and GN-2020B-Q-209), a program of NSF's NOIRLab, which is managed by the Association of Universities for Research in Astronomy (AURA) under a cooperative agreement with the National Science Foundation, on behalf of the Gemini Observatory partnership: the National Science Foundation (United States), National Research Council (Canada), Agencia Nacional de Investigación y Desarrollo (Chile), Ministerio de Ciencia, Tecnología e Innovación (Argentina), Ministério da Ciência, Tecnologia, Inovações e Comunicações (Brazil), and Korea Astronomy and Space Science Institute (Republic of Korea) and processed using the Gemini IRAF package. This work was enabled by observations made from the Gemini North telescope, located within the Maunakea Science Reserve and adjacent to the summit of Maunakea. We are grateful for the privilege of observing the Universe from a place that is unique in both its astronomical quality and its cultural significance. We thank Dr. Mark Jesus Mendoza Magbanua (University of California San Francisco), Jay

Kueny (Steward Observatory, Lowell Observatory), and Prof. David Trilling (NAU) for their encouragement and support during the data reduction phase of this work. We thank Prof. Mike Gowanlock (NAU) for his insights into parallel computing and Monsoon cluster administrator Christopher Coffey (NAU) and the High Performance Computing Support team for facilitating the computational needs during the photometry phase of this work. This material is based upon work supported by the National Science Foundation Graduate Research Fellowship Program under Grant No. (2018258765). C. O. Chandler and C. A. Trujillo also acknowledge support from the NASA Solar System Observations program (Grant 80NSSC19K0869). Computational analyses were run on Northern Arizona University's Monsoon computing cluster, funded by Arizona's Technology and Research Initiative Fund. This work was made possible in part through the State of Arizona Technology and Research Initiative Program. World Coordinate System (WCS) corrections facilitated by the *Astrometry.net* software suite. We thank to R. Vervack for helping to prepare for and participating in the Keck observations. The Telescopio Nazionale Galileo is operated on the island of La Palma by the Centro Galileo Galilei of the INAF (Istituto Nazionale di Astrofisica) at the Spanish Observatorio del Roque de los Muchachos of the Instituto de Astrofísica de Canarias. The observations of Didymos were obtained within the program TNG AOT42_8. E. Mazzotta Epifani, E. Dotto., S. Ieva and M. Dall'Ora acknowledge funding by ASI (Agenzia Spaziale Italiana) under A.A. n. 2019-31-HH.0. D. Souami thanks the Action Fédératrice "ESTERS – Environnement Spatial de la Terre: Recherche & Surveillance" of the Paris Observatory for financial support.

Funding for SDSS-III has been provided by the Alfred P. Sloan Foundation, the Participating Institutions, the National Science Foundation, and the U.S. Department of Energy Office of Science. The SDSS-III web site is http://www.sdss3.org/. SDSS-III is managed by the Astrophysical Research Consortium for the Participating Institutions of the SDSS-III Collaboration including the University of Arizona, the Brazilian Participation Group, Brookhaven National Laboratory, Carnegie Mellon University, University of Florida, the French Participation Group, the German Participation Group, Harvard University, the Instituto de Astrofisica de Canarias, the Michigan State/Notre Dame/JINA Participation Group, Johns Hopkins University, Lawrence Berkeley National Laboratory, Max Planck Institute for Astrophysics, Max Planck Institute for Extraterrestrial Physics, New Mexico State University, New York University, Ohio State University, Pennsylvania State University, University of Portsmouth, Princeton University, the Spanish Participation Group, University of Tokyo, University of Utah, Vanderbilt University, University of Virginia, University of Washington, and Yale University.

APPENDIX

A Fourier series coefficients of Didymos lightcurve decompositions

In Table A.1, we present the coefficients of the best-fit Fourier series (Eq. 1) of the 13 lightcurve decompositions presented in Section 3. For each data set, the table gives the periods, the epoch (the zero point time in asterocentric frame, i.e., with the times corrected for light-travel time, Julian Date; t_0), the mean light level (corresponding to C_0) on the relative magnitude scale for each individual data set, and the normalized Fourier coefficients for the individual orders (up to the maximum significant order; see Section 3). In two cases —the data sets 2019-03-09 to 2019-03-11 and 2021-01-12 to 2021-01-14—, we present the fits done with setting $P_2 = 5.9585$ h, i.e., at half of the assumed synchronous synodic secondary rotation period, as there was apparent a (marginally) significant secondary rotational lightcurve signal (see the analysis in Section 4).

Table A.1: Fourier series coefficients of Didymos lightcurve decompositions

	j	k	C_{jk}/C_0	S_{jk}/C_0
Data 2015-04-13 to 2015-04-14 (Fig. 1)				
$P_1 = 2.2593$ **h**				
$P_2 = 11.91$ **h**				
Epoch = 2457126.05				
Mean Level (mag) $= -2.2440$				
	1	**1**	0.0130	−0.0056
	1	**2**	0.0103	0.0078
	1	**3**	−0.0056	−0.0086
	1	**4**	0.0005	−0.0029
	1	**5**	0.0077	−0.0046
	1	**6**	0.0019	−0.0017
	1	**7**	−0.0041	0.0063
	1	**8**	−0.0062	0.0034
Data 2017-02-23 to 2017-03-01 (Fig. 2)				
$P_1 = 2.2600$ **h**				
$P_2 = 11.917$ **h**				
Epoch = 2457809.58				
Mean Level (mag) $= 18.1804$				

	j	k	C_{jk}/C_0	S_{jk}/C_0
	1	**1**	−0.0227	−0.0078
	1	**2**	0.0012	0.0189
	1	**3**	−0.0026	0.0125
	1	**4**	0.0105	−0.0016
	1	**5**	−0.0023	0.0036
	1	**6**	0.0020	0.0014
	1	**7**	0.0043	0.0031
Data 2017-03-31 to 2017-04-02 (Fig. 3)				
$P_1 = 2.2600$ **h**				
$P_2 = 11.917$ **h**				
Epoch = 2457809.58				
Mean Level (mag) = 18.1941				
	1	**1**	−0.0119	−0.0100
	1	**2**	−0.0139	0.0206
	1	**3**	−0.0038	−0.0002
	1	**4**	0.0018	−0.0026
	1	**5**	0.0077	−0.0015
	1	**6**	−0.0117	0.0055
Data 2017-04-18 to 2017-05-04 (Fig. 4)				
$P_1 = 2.2600$ **h**				
$P_2 = 11.917$ **h**				
Epoch = 2457809.58				
Mean Level (mag) = 18.1969				
	1	**1**	−0.0061	−0.0226
	1	**2**	−0.0180	−0.0024
	1	**3**	−0.0118	−0.0074
	1	**4**	−0.0011	−0.0007
	1	**5**	0.0053	0.0019
	1	**6**	0.0032	0.0011
	1	**7**	0.0003	0.0076
Data 2019-01-31 to 2019-02-02 (Fig. 5)				
$P_1 = 2.2600$ **h**				
$P_2 = 11.917$ **h**				
Epoch = 2458514.96				

	j	k	C_{jk}/C_0	S_{jk}/C_0
Mean Level (mag) $= 19.0530$				
	1	**1**	0.0150	0.0113
	1	**2**	−0.0190	0.0169
	1	**3**	0.0093	−0.0066
	1	**4**	0.0050	0.0092
	1	**5**	0.0029	0.0010
	1	**6**	0.0017	−0.0027
	1	**7**	0.0026	0.0021
Data 2019-03-09 to 2019-03-11 (Fig. 6)				
$P_1 = 2.2600$ **h**				
$P_2 = 5.9585$ **h**				
Epoch = 2458552.82				
Mean Level (mag) $= 19.0618$				
	1	**1**	0.0141	0.0136
	1	**2**	−0.0134	0.0082
	1	**3**	0.0066	0.0016
	1	**4**	0.0019	0.0024
	1	**5**	−0.0018	−0.0005
	1	**6**	0.0016	−0.0007
	1	**7**	−0.0010	0.0009
	1	**8**	0.0003	−0.0012
	1	**9**	−0.0004	0.0017
	2	**1**	−0.0069	0.0049
Data 2020-12-12 to 2020-12-23 (Fig. 7)				
$P_1 = 2.2602$ **h**				
$P_2 = 11.917$ **h**				
Epoch = 2459224.31				
Mean Level (mag) $= 19.5426$				
	1	**1**	−0.0216	0.0000
	1	**2**	−0.0078	0.0348
	1	**3**	0.0058	0.0199
	1	**4**	0.0116	−0.0090
	1	**5**	−0.0002	0.0075

	j	k	C_{jk}/C_0	S_{jk}/C_0
	1	**6**	−0.0020	0.0010
Data 2021-01-08 to 2021-01-10 (Fig. 8)				
$P_1 = 2.2602$ **h**				
$P_2 = 11.917$ **h**				
Epoch = 2459224.31				
Mean Level (mag) = 19.5439				
	1	**1**	−0.0173	0.0013
	1	**2**	−0.0089	0.0287
	1	**3**	0.0061	0.0171
	1	**4**	0.0101	−0.0069
	1	**5**	0.0009	0.0049
	1	**6**	−0.0053	0.0024
	1	**7**	0.0022	0.0030
Data 2021-01-12 to 2021-01-14 (Fig. 9)				
$P_1 = 2.2602$ **h**				
$P_2 = 5.9585$ **h**				
Epoch = 2459224.31				
Mean Level (mag) = 19.5450				
	1	**1**	−0.0161	−0.0009
	1	**2**	−0.0055	0.0258
	1	**3**	0.0034	0.0150
	1	**4**	0.0110	−0.0068
	1	**5**	−0.0010	0.0034
	1	**6**	−0.0044	0.0017
	1	**7**	0.0003	0.0030
	1	**8**	0.0017	0.0019
	2	**1**	0.0004	0.0037
Data 2021-01-17 to 2021-01-18 (Fig. 10)				
$P_1 = 2.2602$ **h**				
$P_2 = 11.917$ **h**				
Epoch = 2459224.31				
Mean Level (mag) = 19.5138				
	1	**1**	−0.0242	−0.0003
	1	**2**	−0.0087	0.0266

	j	k	C_{jk}/C_0	S_{jk}/C_0
	1	**3**	0.0009	0.0171
	1	**4**	0.0101	−0.0053
	1	**5**	0.0030	0.0024
	1	**6**	−0.0036	0.0024
	1	**7**	0.0009	0.0016
	1	**8**	0.0015	0.0018
Data 2021-01-20 (Fig. 11)				
$P_1 = 2.2602$ **h**				
$P_2 = 11.917$ **h**				
Epoch = 2459224.31				
Mean Level (mag) = 19.5146				
	1	**1**	−0.0187	0.0013
	1	**2**	−0.0088	0.0244
	1	**3**	−0.0006	0.0183
	1	**4**	0.0102	−0.0048
	1	**5**	−0.0002	0.0022
	1	**6**	−0.0048	0.0012
Data 2021-02-17 (Fig. 12)				
$P_1 = 2.2602$ **h**				
$P_2 = 11.917$ **h**				
Epoch = 2459224.31				
Mean Level (mag) = 19.5325				
	1	**1**	−0.0104	−0.0111
	1	**2**	−0.0088	0.0086
	1	**3**	0.0009	0.0049
	1	**4**	0.0040	0.0034
	1	**5**	0.0032	−0.0033
Data 2021-03-06 (Fig. 13)				
$P_1 = 2.2602$ **h**				
$P_2 = 11.917$ **h**				
Epoch = 2459224.31				
Mean Level (mag) = 19.5393				
	1	**1**	−0.0093	−0.0070
	1	**2**	−0.0147	0.0130

j	k	C_{jk}/C_0	S_{jk}/C_0
1	**3**	−0.0072	0.0050
1	**4**	0.0031	0.0022
1	**5**	0.0017	−0.0003
1	**6**	−0.0030	−0.0026

References

Ahn, C. P., Alexandroff, R., Allende Prieto, C., et al. 2012, ApJS, 203, 21
Ahumada, R., Prieto, C. A., Almeida, A., et al., 2020, ApJS, 249, 3
Appenzeller, I., Fricke, K., Fürtig, W., et al. 1998, Msngr, 94, 1
Astropy Collaboration, Price-Whelan, A. M., Sipöcz, B. M., et al. 2018, AJ, 156, 123
Bertin, E. 2006, ASPC, 351, 112
Bertin, E. & Arnouts, S. 1996, A&AS 117, 393
Binzel, R. P., Rivkin, A. S., Stuart., J. S., et al. 2004, Icar, 170, 259
Blanton, M. R., Bershady, M. A., Abolfathi, B., et al., 2017, AJ, 154, 28
Bradley, L., Sipöcz, B., Robitaille, T., et al. 2017, Astropy/Photutils: V0.4. Zenodo. DOI: 10.5281/zenodo.1039309
Buzzoni, B., Delabre, B., Dekker, H., et al. 1984, Msngr, 38, 9
Cepa, J. 2010, In: Highlights of Spanish Astrophysics V, eds. J.M. Diego & L. J. Goicoechea, 15
Cepa, J., Aguiar, M., Escalera, V. G., et al. 2000, 2000SPIE 4008, 623
Chambers, K. C., Magnier, E. A., Metcalfe, N. et al. 2016, arXiv:1612.05560 [astro-ph.IM]
Chandler, C. O., Curtis, A. M., Mommert, M., Sheppard, S. S. & Trujillo, A. A. 2018, PASP, 130, 114502
Collins, K. A., Kielkopf, J. F., Stassun, K. G. & Hessman, F. V. 2017, AJ, 153, 77
de León, J., Licandro, J., Duffard, R. & Serra-Ricart, M. 2006, ASR,.37, 178
de León, J., Licandro, J., Serra-Ricart, M., Pinlla-Alonso, N. & Campins, H. 2010, A&A, 517, A23
Dotto, E., Delal Corte, V., Amoroso, M., et al. 2021, PSS 199 105185
Dunn, T. L., Burbine, T. H., Bottke Jr, W. F., Clark, J. P. 2013, Icar, 222, 273
Flewelling, H. A., Magnier, E. A., Chambers, K. C., et al. 2020, ApJS, 251, 7
Gaia Collaboration, Brown, A. G. A., Vallenari, A., et al. 2018, A&A, 616, A1
Gaia Collaboration, Brown, A. G. A., Vallenari, A., et al. 2021, A&A, 649, A1
Hook, I. M., Jøorgensen, I., Allington-Smith, J. R., et al. 2004, PASP, 116, 425
Ieva, S., et. al. 2022, PSJ, submitted
Kitazato, K., Abe, M., Mito, H., et al. 2004, 2005LPI 35, 1623
Kokotanekova, R., Snodgrass, C., Lacerda, P., et al. 2017, MNRAS, 471, 2974
Laher, R. R., Gorjian, V., Rebull, L. M., et al. 2012, PASP 124, 737
Lang, D., Hogg, D. W., Mierle, K., Blanton, M. & Roweis, S. 2010, AJ, 139, 1782
Le Févre, O., Sisse, M., Mancini, D., et al., 2003, 2003SPIE 4841, 1670
Lupton R. H., Jurić, M., Ivezić, Z. et al. 2005, BAAS 37 1384

Magnusson, P., Dahlgren, M., Barucci, M. A., et al. 1995, Icar, 123, 227
Michel, P., Kueppers, M., Campo Bagatin, A., et al. 2022, PSJ, submitted
Mommert, M. 2017, A&C, 18, 47
Naidu, S. P., Benner, L. A. M., Brozovic, M., et al. 2020, Icar, 348, 113777
Naidu, S. P., Chesley, S. R., Farnocchia, D., et. al. 2022, PSJ, submitted
Ochsenbein, F., Bauer, P. & Marcourt, J. 2000, A&AS, 143, 23
Pravec, P. & Harris, A. W. 2007, Icar, 190, 250
Pravec, P., Šarounová, L. & Wolf, M. 1996, Icar, 124, 471
Pravec, P., Šarounová, L., Rabinowitz, D. L., et al. 2000, Icar, 146, 190203
Pravec, P., Benner, L. A. M., Nolan, M. C., et al. 2003, IAUC, 8244
Pravec, P., Harris, A. W., Scheirich, P., et al. 2005, Icar, 181, 63
Pravec, P., Scheirich, P., Kušnirák, P., et al. 2016, Icar, 267, 267
Rivkin, A. S., Chabot, N. L., Stickle, A. M., et al. 2021, PSJ, 2, 173
Scheirich, P. & Pravec, P. 2009, Icar, 200, 531
Scheirich, P. & Pravec, P. 2022, PSJ, **in press**
Schirmer, M. 2013, ApJS, 209, 21
Snodgrass, C., Saviane, I., Monaco, L. & Sinclaire, P. 2008, Msngr, 132, 18
Stetson, P. B. 1987, PASP, 99, 191
Stetson, P. B. 1990, PASP, 102, 932
Stetson, P. B. 1993, 1993spct conf, 291
Taylor, M. B. 2006, ASPC, 351, 666
Thirouin, A. & Sheppard, S. 2018, AJ, 155, 248
Thirouin, A., Moskovitz, N. A., Binzel, R. P., et al. 2018, ApJS, 239, 4
Tody, D. 1986, 1986SPIE 627, 733
Tody, D., 1993. 1993APPC 52, 173
Tonry, J. L., Stubbs, C. W., Lykke, K. R., et al. 2012. ApJ, 750, 99
Zappalà, V., Cellino, A., Barucci, A. M., Fulchignoni, M. & Lupishko, D. F.
1990. A&A, 231, 548